

# Time-lapse monitoring of seismic velocity associated with 2011 Shinmoe-dake eruption using seismic interferometry

Kiwamu Nishida<sup>1,1</sup>, Yuta Mizutani<sup>2,2</sup>, Mie Ichihara<sup>1,1</sup>, and Yosuke Aoki<sup>1,1</sup>

<sup>1</sup>University of Tokyo

<sup>2</sup>JX Nippon Oil & Gas Exploration Corp

November 30, 2022

## Abstract

Seismic interferometry is a powerful tool to monitor the seismic velocity change associated with volcanic eruptions. For the monitoring, changes in seismic velocity with environmental origins (such as precipitation) are problematic. In order to model the environmental effects, we propose a new technique based on a state-space model. An extended Kalman filter estimates seismic velocity changes as state variables, with a first-order approximation of the stretching method. We apply this technique to three-component seismic records in order to detect the seismic velocity change associated with the Shinmoe-dake eruptions in 2011 and 2018. First, ambient noise cross-correlations were calculated from May 2010 to April 2018. We also modeled seismic velocity changes resulting from precipitation and the 2016 Kumamoto earthquake, with exponential type responses. Most of the results show no significant changes associated with the eruptions, although gradual inflation of the magma reservoir preceded the 2011 eruption by one year. The observed low sensitivity to static stress changes suggests that the fraction of geofluid and crack density at about 1 km depth is small, and the crack shapes could be circular. Only one station pair west of the crater shows the significant drop associated with the eruption in 2011. The gradual drop of seismic velocity up to 0.05% preceded the eruption by one month. When the gradual drop began, volcanic tremors were activated at about 2 km depth. These observations suggest that the drop could be caused by damage accumulation due to vertical magma migration beneath the summit.

1     **Time-lapse monitoring of seismic velocity associated**  
2             **with 2011 Shinmoe-dake eruption using seismic**  
3             **interferometry: an extended Kalman filter approach**

4             **Kiwamu Nishida<sup>1</sup>, Yuta Mizutani<sup>1,2</sup>, Mie Ichihara<sup>1</sup>, Yosuke Aoki<sup>1</sup>**

5             <sup>1</sup>Earthquake Research Institute, University of Tokyo, 1-1-1 Yayoi 1, Bunkyo-ku, Tokyo 113-0032, Japan  
6                             <sup>2</sup>JX Nippon Oil & Gas Exploration Corp.

7             **Key Points:**

- 8             • A new technique of an extended Kalman filterz for estimating the temporal change  
9             of seismic velocity is developed.  
10            • Mass variations in the subsurface due to precipitation can explain observed sea-  
11            sonal variations in seismic velocity.  
12            • Spatial and temporal variations in seismic velocity suggest that damage due to  
13            magma migration could be the origin.

---

Corresponding author: Kiwamu Nishida, [knishida@eri.u-tokyo.ac.jp](mailto:knishida@eri.u-tokyo.ac.jp)

## Abstract

Seismic interferometry is a powerful tool to monitor the seismic velocity change associated with volcanic eruptions. For the monitoring, changes in seismic velocity with environmental origins (such as precipitation) are problematic. In order to model the environmental effects, we propose a new technique based on a state-space model. An extended Kalman filter estimates seismic velocity changes as state variables, with a first-order approximation of the stretching method. We apply this technique to three-component seismic records in order to detect the seismic velocity change associated with the Shinmoe-dake eruptions in 2011 and 2018. First, ambient noise cross-correlations were calculated from May 2010 to April 2018. We also modeled seismic velocity changes resulting from precipitation and the 2016 Kumamoto earthquake, with exponential type responses. Most of the results show no significant changes associated with the eruptions, although gradual inflation of the magma reservoir preceded the 2011 eruption by one year. The observed low sensitivity to static stress changes suggests that the fraction of geofluid and crack density at about 1 km depth is small, and the crack shapes could be circular. Only one station pair west of the crater shows the significant drop associated with the eruption in 2011. The gradual drop of seismic velocity up to 0.05% preceded the eruption by one month. When the gradual drop began, volcanic tremors were activated at about 2 km depth. These observations suggest that the drop could be caused by damage accumulation due to vertical magma migration beneath the summit.

## 1 Introduction

Shinmoe-dake forms part of a group of Kirishima volcanoes, located in Kyusyu Japan, and is an active volcano. Over a period of ten years, it experienced a major eruption in 2011, and a effusive eruption in 2018. In 2011, the eruptive sequence started with sub-Plinian eruptions (January 26-27th), followed by a lava effusion (January 28-31st), and culminating in Vulcanian eruptions (1-10 Feb.) (Nakada et al., 2013). Observations from Global Navigation Satellite Systems (GNSS) show that the gradual inflation of the magma reservoir preceded the 2011 eruption by one year. The magma reservoir is located approximately 7 km northwest of Shinmoe-dake at a depth of approximately 8 km below sea level (BSL) (Nakao et al., 2013; Kozono et al., 2013). When the inflation started, low-frequency earthquakes (LFE) at a depth of 20-27 km was activated, suggesting the migration of magma from a deeper region (Kurihara et al., 2019). During the 2011 eruptions, the GNSS data indicate the co-eruption deflation of the magma reservoir. Tilt observation showed an-hour-long inflation and rapid deflation at a shallow depth (around 500 m) near the summit right before the first sub-Plinian event (Takeo et al., 2013). Also stepwise local tilt inflations were reported twice in about a week before the sub-Plinian event (Ichihara & Matsumoto, 2017). During the eruption, explosion earthquakes were observed (Nakamichi et al., 2013). The activities suggest that the magma touched an aquifer at shallow depths of about -1.0 km BSL (e.g., Kagiya et al., 1996). Before and during the sub-Plinian eruptions, migration of gas (probably with magma) also activated continuous volcanic tremors (Ichihara & Matsumoto, 2017). These were located beneath the crater for one week before the major eruption, and they rose from a depth of a few kilometers to the near-surface aquifer three times. The heat transported to the water layer could have triggered the sub-Plinian eruptions (Ichihara & Matsumoto, 2017). In order to understand the magma plumping system, pertinent information from depths of 1 to 10 km is crucial. However, we could not detect earthquake activity at these depths before the major eruptions associated with the magma migration (Ueda et al., 2013) and other geophysical phenomena.

Seismic interferometry is a powerful technique for monitoring seismic velocity in the depth range of interest. In recent years, the number of applications of seismic interferometry has increased. In the analysis, the cross-correlation function between ambient noise records of a pair of stations can be regarded as a virtual seismic waveform, recorded

at one station when the source is placed at the other station. In any time period, the seismic velocity around the station pair can be estimated from the cross-correlation function calculated without an earthquake; thus, seismic interferometry has been applied in many studies to monitor temporal changes in seismic velocity (e.g., Obermann & Hillers, 2019). This technique has been applied for detecting seismic wave velocity changes after large earthquakes (e.g., Wegler & Sens-Schönfelder, 2007; Wegler et al., 2009; Brenguier, Campillo, et al., 2008; Brenguier et al., 2014), those of a slow slip event (Rivet et al., 2011), and those associated with volcanic eruptions: e.g., the Piton de La Fournaise volcano, La Réunion, France (Brenguier, Shapiro, et al., 2008), Mt. Asama, Japan (Nagaoka et al., 2010), Merapi volcano, Indonesia (Budi-Santoso & Lesage, 2016), Ubinas volcano, Peru (Machacca et al., 2019), and Kilauea volcano, USA (Donaldson et al., 2017). For example, Brenguier, Shapiro, et al. (2008) detected a drop in seismic velocity of the order of 0.1% for a number of days preceding the eruption of the Piton de La Fournaise volcano, and the velocity recovered at a time scale of about 10-20 days. There are two potential mechanisms for the temporal changes (Olivier et al., 2019). The first is pressurization due to the magma migration in a linear elastic regime. In this regime, stress sensitivity of seismic velocity change is a proxy for inferring the state of the material: in particular the existence of geofluid (Brenguier et al., 2014). The second is damage accumulation beyond the linear elastic regime.

The biggest technical difficulty in monitoring is the separation of temporal variations of volcanic origin from environmental variations. Many researchers reported seasonal variations associated with environmental phenomena: rainfall (e.g., Rivet et al., 2015), air pressure (e.g., Niu et al., 2008), and thermo-elasticity (e.g., Hillers, Ben-Zion, et al., 2015). In the region of Mt. Shimoe-dake, daily precipitation exceeds 100 mm for several days in a year, while the annual precipitation is more than 4000 mm. Wang et al. (2017) reported that rainfall is the major source of the observed temporal changes in this area (Kyusyu). The Merapi Volcano, Indonesia, Sens-Schönfelder and Wegler (2006) also experienced the observed dominance of seasonal variations. Temporal changes in groundwater levels based on precipitation data can explain the observed strong seasonal variations in both cases. Such strong seasonal variations have the potential to mask a temporal change associated with volcanic activities; thus, correction for rainfall is crucial for inferring the temporal changes associated with volcanic activity (Rivet et al., 2015; Wang et al., 2017).

Earthquakes also contaminate temporal changes in seismic velocities associated with volcanic activities. In particular, this region experienced the 2016 Kumamoto earthquake of Mw 7.3 (e.g., Kato et al., 2016). The seismic-velocity dropped during the earthquake, and recovered over a time scale of several months (Nimiya et al., 2017). Since the seismic-velocity reduction on the order of 0.1% could be comparable to typical temporal variations associated with volcanic activities, it should be subtracted. Moreover, the susceptibility, which is defined by the ratio between observed reductions in seismic velocity and the estimated dynamic stress (Brenguier et al., 2014), is a good proxy for discussing the state of geofluid in the upper crust associated with a volcanic process.

In this study, we introduce an empirical Bayes approach to separate the effects of precipitation and the earthquake from the observed seismic velocity changes to extract those of volcanic origins (Malinverno & Briggs, 2004). It has two levels of inference. At the lower level, the seismic velocity changes were modeled in a state-space form. An extended Kalman filter/smoothing (section 4) estimates seismic velocity changes as state variables. Precipitation and earthquake effects are modeled as explanatory variables, which are deterministic at this level. At the higher level, hyper-parameters (model covariance, data covariance, and explanatory variables) are estimated by the Maximum Likelihood Method (section 5). This two-level approach has the following features: (1) we can constrain the hyper-parameters from data directly. (2) we can evaluate the separation of the origins in a statistical manner, (3) the approach gives us a criterion of the model selec-

119 tion (see section 5.3 for details) and (4) the extended Kalman filter/smoothing is numerically efficient. Notation section at the end of this paper provides a list of definitions  
 120 of the variables used in this paper.  
 121

122 We combine the extracted temporal velocity changes of volcanic origins with the  
 123 geodetic observation and volcanic tremor activity to discuss the magma migration in section 6.  
 124

## 125 2 Cross-correlation analysis

126 We used three component seismograms recorded at eight stations (six broadband  
 127 sensors and two short-period sensors with a natural frequency of 1 Hz) from May 1st,  
 128 2010 to April 30th, 2018, shown in Figure 1. Five stations were deployed by the Earth-  
 129 quake Research Institute, the University of Tokyo, and the other three were deployed  
 130 by the National Research Institute for Earth Science and Disaster Prevention (NIED).  
 131 The details of the sensors are shown in Table 1. We used daily precipitation data recorded  
 132 by a station (Ebino shown by the white circle in Figure 1) of the Japan Meteorological  
 133 Agency (JMA) for correcting the precipitation effects as described in section 5.1.

134 First, the data were down-sampled from 100 Hz to 2.5 Hz. The instrumental re-  
 135 sponses were corrected in time domain (Maeda et al., 2011) according to the sensor type,  
 136 and all records were bandpass-filtered from 0.15 to 0.90 Hz. For each station pair, the  
 137 two horizontal components were rotated into radial and transverse coordinates accord-  
 138 ing to the geometry of the station pair: the radial direction is parallel to the great circle  
 139 path between the station pair, and the transverse direction is perpendicular to the  
 140 great circle path (Nishida et al., 2008). The daily records were divided into segments of  
 141 409.6 s, with an overlap of 204.8 s.

142 To reject noisy data, which include transient phenomena such as high instrumen-  
 143 tal noise or earthquakes, we discarded the noisy segments as follows. For one-day data  
 144 of each component at a station, we estimated the root mean squared amplitudes (RMSs)  
 145 of all the segments. For each component of one-day data, we defined the threshold to  
 146 be twice the median value of RMSs for all the segments in one day. If the RMS of a seg-  
 147 ment was larger than the threshold, the segment was discarded.

Network	Station name	Sensor type
ERI	KVO	L4-C (1 s, -2/2/2011), Trillium-120 (120 s, 2/3/2011-)
ERI	SMN	Trillium-40 (40 s, -7/22/2010) Trillium-120 (120 s, 7/23/2010-)
ERI	SMW	L4-C (1 s)
ERI	TKW	CMG3T (100 s)
ERI	TKS	Trillium-40 (40 s, -2/4/2011) Trillium-120 (120 s, 2/5/2011-)
NIED (V-net)	KRHV	Trillium-240 (240 s)
NIED (V-net)	KRMV	Trillium-240 (240 s)
NIED (Hi-net)	MJNH	Hi-net 1 Hz velocity meter (1 s)

**Table 1.** Sensor type for each station. ERI represents a station deployed by the Volcano Research Center, Earthquake Research Institute, the University of Tokyo. NIED (V-net) means a station of the Volcano Observation network deployed by the National Research Institute for Earth Science and Disaster Prevention, and NIED (Hi-net) means a station of High-Sensitivity Seismograph Network deployed by NIED.

148 We then took cross-correlation functions (CCFs) of all possible pairs of stations,  
 149 and all possible component combinations for each station pair with the spectral whiten-

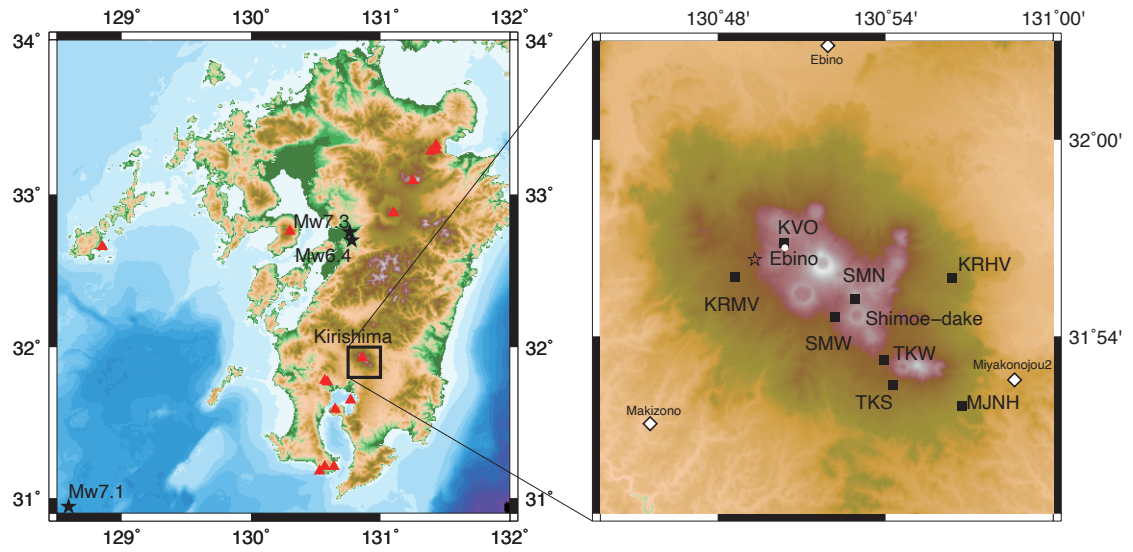


**Figure 1.** Left: Red triangles show active volcanoes. Black stars represent the hypocenters of earthquakes: (i) Mw 6.4, April 14th (UTC), 2016, the foreshock of the Kumamoto earthquake, (ii) Mw 7.3, April 15th (UTC), 2016, the mainshock of the Kumamoto earthquake and (ii) Mw 7.1, November 13th (UTC), 2015, the Satsuma earthquake. Right: Station distribution. Black squares show station locations, and the white circle shows the JMA weather station. Three white diamond symbols show the locations of GEONET stations operated by the Geospatial Information Authority of Japan. The star symbol shows the location of a volumetric source at a depth of 8.35 km (Nakao et al., 2013). The topography in the right panel is given by the corresponding Shuttle Radar Topography Mission (Farr et al., 2007).

150 ing, as done in previous studies (Bensen et al., 2007). We stacked the CCFs of the se-  
 151 lected segments over one day. The daily CCFs of the individual pairs of stations were  
 152 represented by  $\phi_t^p(\tau)$ , where  $\tau$  shows lag time, and the subscript  $t$  is an integer, which  
 153 represents days from 1 May 2010 (JST), and the superscript  $p$  shows the pair of compo-  
 154 nents (9 components:  $R-R$ ,  $R-T$ , ...,  $Z-Z$ , where  $R$  is the radial component,  
 155 and  $T$  is transverse component, and  $Z$  is vertical component). Figure 2 shows a typi-  
 156 cal example of daily CCFs, which are stable even in their coda parts for eight years. Fig-  
 157 ure 3 shows a typical example of the mean power spectrum of the mean CCF between  
 158 a pair of broadband stations, which shows dominance in lower frequencies from 0.25-0.5  
 159 Hz, even after the spectral whitening.

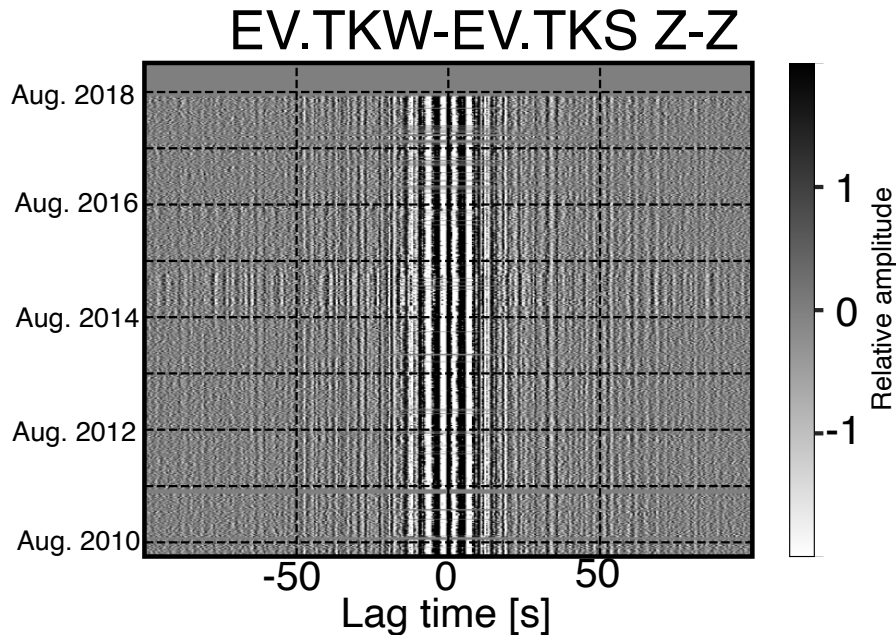


**Figure 2.** Daily CCFs of Z-Z component (0.2-0.4 Hz) between TKS and TKW. The vertical axis shows date, the horizontal axis shows lag time.

### 160 3 Measurements of seismic velocity change

161 Seismic interferometry is feasible for monitoring seismic wave velocity between pairs  
 162 of stations. The principle of seismic interferometry is that the CCF between a station  
 163 pair represents the seismic wavefield as though a source lies at one station and a receiver  
 164 lies at the other. However, the disadvantage of this technique is that the measurements  
 165 are overly sensitive to source heterogeneity (e.g., Weaver et al., 2009). This causes a trade-  
 166 off between a temporal change of seismic velocity and that of source heterogeneity. Al-  
 167 though the direct waves are sensitive to the source heterogeneity, the coda part becomes  
 168 insensitive with increasing lapse time. This is because the seismic wavefield loses the source  
 169 information over multiple scatterings (Colombi et al., 2014). If the seismic velocity changes  
 170 uniformly in space, the arrival time delays with lapse time. This approach is known as  
 171 the doublet method in frequency domain, first applied to earthquake coda (Poupinet et  
 172 al., 1984). This method is also feasible for monitoring of seismic velocity with seismic  
 173 interferometry (e.g., Brenguier et al., 2014; Hillers, Husen, et al., 2015). We used the method  
 174 in the time domain, known as the stretching method (Weaver & Lobkis, 2000), because

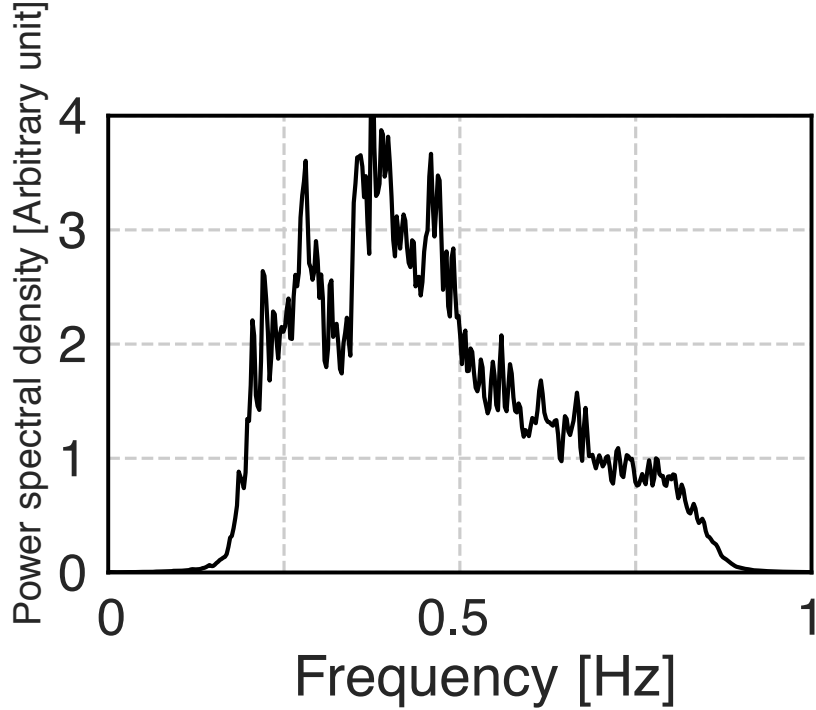


**Figure 3.** Power spectrum averaged over all CCFs between TKS and TKW with the time window from -99.6 to -20 s and from 20 to 99.6 s.

175 the linearization is easier for an application of an extended Kalman filter as described  
 176 in the next section.

177 We constructed a model function,  $m^p(A_t, \gamma_t; \tau)$ , for the observed CCF  $\phi_t^p(\tau)$  by stretch-  
 178 ing the reference CCF  $\varphi_{ref}^p(\tau)$  as,

$$179 \quad m^p(A_t, \gamma_t; \tau) = A_t \varphi_{ref}^p(\tau(1 + \gamma_t)), \quad (1)$$

180 where  $\gamma_t$  is the stretching factor,  $A_t$  is amplitude and the subscript  $t$  represents day. The  
 181 preliminary reference CCF  $\varphi_{ref}^p(\tau)$  was estimated by averaging all the observed CCFs  
 182  $\phi_t^p(\tau)$  over days  $t$  (see section 4.1).

183 To estimate the temporal evolution of  $\gamma_t$ , Weaver and Lobkis (2000) constructed  
 184 a dilation correlation coefficient between waveforms  $X^p$  as,

$$185 \quad X^p(\gamma_t) = \frac{\int \phi_t^p(\tau) m^p(A_t, \gamma_t; \tau) d\tau}{\sqrt{\int \phi_t^p(\tau)^2 d\tau} \sqrt{\int (m^p(A_t, \gamma_t; \tau))^2 d\tau}}. \quad (2)$$

186 By maximizing the correlation, the temporal variation  $\gamma_t$  can be estimated. Several re-  
 187 searchers have used this method to measure the temporal changes in seismic velocity.  
 188 To enhance the signal to noise ratio, measurements over many station pairs and com-  
 189 ponents were averaged. Bayesian approaches (Tarantola & Valette, 1982) for these mea-  
 190 surements are feasible for more reliable estimations (Brenouier et al., 2016).

191 To enhance the flexibility of the Bayesian approach, we developed a new method  
 192 of an extended Kalman filter based on the state-space model (e.g., Segall & Matthews,  
 193 1997; Durbin & Koopman, 2012). This method, successively, minimizes the squared dif-  
 194 ference given by

$$195 \quad S(A_t, \gamma_t) \equiv \int (\phi_t^p(\tau) - m^p(A_t, \gamma_t; \tau))^2 d\tau. \quad (3)$$

196  $A_t$  and  $\gamma_t$  are recognized as state variables for the state modeling as shown in the next  
 197 section.

198 In sections 4 and 5, we introduce an empirical Bayes approach to minimize the squared  
 199 difference. It has two levels of inference. At the lower level, the seismic velocity changes  
 200 were modeled in a state-space form. An extended Kalman filter/smoothen (section 4)  
 201 estimates seismic velocity changes as state variables. At the higher level, hyper-parameters  
 202 (model covariance, data covariance, and explanatory variables for precipitation and earth-  
 203 quake effects) are estimated by the Maximum Likelihood Method (section 5).

#### 204 4 State Space modeling using an extended Kalman filter approach

205 Here we considered state variables  $\alpha_t$ , which describe the amplitude  $A_t$  and the  
 206 stretching factor  $\gamma_t$  at  $t = 1, \dots, n$  assuming that the state variables are common to  
 207 all the 9 components for each station pair. The state variables and the data vector of  
 208 observed CCF  $\mathbf{y}_t^p$  for a  $p$ th component are defined by

$$209 \quad \alpha_t \equiv \begin{pmatrix} A_t \\ \gamma_t \end{pmatrix}, \mathbf{y}_t^p \equiv \begin{pmatrix} \phi_t^p(-\tau_e) \\ \vdots \\ \phi_t^p(-\tau_s) \\ \phi_t^p(\tau_s) \\ \vdots \\ \phi_t^p(\tau_e) \end{pmatrix}, \quad (4)$$

210 where  $\tau_s$  is the start of lag time (20 s) and  $\tau_e$  is the end of lag time (99.6 s). They obey  
 211 the following relations:

$$212 \quad \mathbf{y}_t^p = \mathbf{m}^p(\alpha_t + \mathbf{R}_t + \mathbf{E}_t) + \epsilon_t, \quad \epsilon_t \sim \mathcal{N}(0, \mathbf{H}_t) \quad (5)$$

$$213 \quad \alpha_{t+1} = \alpha_t + \boldsymbol{\eta}_t, \quad \boldsymbol{\eta}_t \sim \mathcal{N}(0, \mathbf{Q}_t). \quad (6)$$

215 Here we introduce explanatory variables  $\mathbf{R}_t$  related to precipitation and  $\mathbf{E}_t$  associated  
 216 with the seismic-velocity drop during the 2016 Kumamoto earthquake based on Wang  
 217 et al. (2017), respectively. Because the explanatory variables are recognized as hyper-  
 218 parameters in this study, they are deterministic at this level. Subsequently, they are es-  
 219 timated by Maximum Likelihood Method at the higher level (see section 5 for details).  
 220 Section 5.3 also shows how to choose explanatory variables based on likelihood.  $\epsilon_t$  and  
 221  $\boldsymbol{\eta}_t$  are mutually independent random variables, subject to normal distribution ( $\mathcal{N}$ ) with  
 222 zero means and covariance matrix  $\mathbf{H}_t$  and  $\mathbf{Q}_t$ , respectively. The model  $\mathbf{m}^p$  are defined  
 223 by

$$224 \quad \mathbf{m}^p(\alpha_t + \mathbf{R}_t + \mathbf{E}_t) \equiv \begin{pmatrix} m^p(\alpha_t + \mathbf{R}_t + \mathbf{E}_t; -\tau_e) \\ \vdots \\ m^p(\alpha_t + \mathbf{R}_t + \mathbf{E}_t; -\tau_s) \\ m^p(\alpha_t + \mathbf{R}_t + \mathbf{E}_t; \tau_s) \\ \vdots \\ m^p(\alpha_t + \mathbf{R}_t + \mathbf{E}_t; \tau_e) \end{pmatrix}. \quad (7)$$

225 Since the sampling interval of CCFs is 0.4 s, the dimension of the vectors  $\mathbf{y}_t^p$  and  $\mathbf{m}^p$  is  
 226  $2 \cdot ((\tau_e - \tau_s)/0.4 + 1) = 400$ . With an assumption of the constant data covariance with  
 227 respect to time and lag time,  $\mathbf{H}_t$  can be written by a diagonal matrix:

$$228 \quad \mathbf{H}_t \equiv h_0 \mathbf{I}, \quad (8)$$

229 where  $h_0$  is a prior data covariance and  $\mathbf{I}$  is the  $400 \times 400$  identity matrix. Assuming  
 230 that the amplitude  $A_t$  does not correlate with the seismic velocity change  $\gamma_t$ , we can write  
 231  $\mathbf{Q}_t$  as a diagonal matrix:

$$232 \quad \mathbf{Q}_t \equiv \begin{pmatrix} q_0 & 0 \\ 0 & q_1 \end{pmatrix}, \quad (9)$$

233 where  $q_0$  and  $q_1$  are a prior model covariance.  $h_0$  is estimated from the time average of  
 234 the squared difference between  $\phi_t^p(\tau)$  and the reference  $\varphi_{ref}^p(\tau)$ . Since the amplitude  $A_t$   
 235 is a kind of normalization factor, it is difficult to separate the origins: volcanic, precip-  
 236 itation, or earthquake. For simplicity, we omitted the amplitude term  $A_t$  for precipita-  
 237 tion and earthquakes. Accordingly  $\mathbf{R}_t$  and  $\mathbf{E}_t$  are given by,

$$238 \quad \mathbf{R}_t \equiv \begin{pmatrix} 0 \\ r_t \end{pmatrix}, \mathbf{E}_t \equiv \begin{pmatrix} 0 \\ e_t \end{pmatrix}. \quad (10)$$

239 The state variable  $\boldsymbol{\alpha}_t$  has an initial value  $\mathbf{a}_1$  at  $t = 1$  subject to a normal dis-  
 240 tribution  $\sim N(\mathbf{a}_1, \mathbf{P}_1)$  defined by

$$241 \quad \mathbf{a}_1 \equiv \begin{pmatrix} A_1 \\ \gamma_1 \end{pmatrix}, \mathbf{P}_1 \equiv \begin{pmatrix} p_0 & 0 \\ 0 & p_1 \end{pmatrix}, \quad (11)$$

242 where  $A_1$  is a prior initial amplitude,  $\gamma_1$  is a prior initial stretching factor,  $p_0$  and  $p_1$  are  
 243 a prior model covariance for the initial value.

244 First, we assumed that  $\mathbf{Q}_t$ ,  $\mathbf{R}_t$ ,  $\mathbf{E}_t$  and  $\mathbf{P}_1$  are given in advance; that is, they are  
 245 recognized as hyper-parameters. At the higher level, we estimated the hyper-parameters  
 246 using the Maximum Likelihood Method as discussed in the next section.

247 We linearized equation (1) (e.g., Weaver et al., 2011) in order to apply the extended  
 248 Kalman filter. We consider the update of state variable from the initial guess  $\hat{\boldsymbol{\alpha}}_t \equiv (\hat{A}_t, \hat{\gamma}_t)^T$ .  
 249 Assuming that the increment from the initial guess  $\Delta\boldsymbol{\alpha}$  is small, Taylor series of  $\mathbf{m}^p$  in  
 250 equation (5) at around the initial guess  $\hat{\boldsymbol{\alpha}}_t$  up to 1st order lead the following equation,

$$251 \quad \mathbf{m}^p(\hat{\boldsymbol{\alpha}}_t + \Delta\boldsymbol{\alpha} + \mathbf{R}_t + \mathbf{E}_t) = \mathbf{m}^p(\hat{\boldsymbol{\alpha}}_t + \mathbf{R}_t + \mathbf{E}_t) + \boldsymbol{\zeta}_t^p \Delta\boldsymbol{\alpha}, \quad (12)$$

252 where

$$253 \quad \boldsymbol{\zeta}_t^p = \begin{pmatrix} \varphi_{ref}^p(-(1 + \hat{\gamma}_t + r_t + e_t)\tau_e) & -\hat{A}_t \tau_e \dot{\varphi}_{ref}^p(-(1 + \hat{\gamma}_t + r_t + e_t)\tau_e) \\ \vdots & \vdots \\ \varphi_{ref}^p(-(1 + \hat{\gamma}_t + r_t + e_t)\tau_s) & -\hat{A}_t \tau_s \dot{\varphi}_{ref}^p(-(1 + \hat{\gamma}_t + r_t + e_t)\tau_s) \\ \varphi_{ref}^p((1 + \hat{\gamma}_t + r_t + e_t)\tau_s) & \hat{A}_t \tau_s \dot{\varphi}_{ref}^p((1 + \hat{\gamma}_t + r_t + e_t)\tau_s) \\ \vdots & \vdots \\ \varphi_{ref}^p((1 + \hat{\gamma}_t + r_t + e_t)\tau_e) & \hat{A}_t \tau_e \dot{\varphi}_{ref}^p((1 + \hat{\gamma}_t + r_t + e_t)\tau_e) \end{pmatrix}, \quad (13)$$

254 and  $\dot{\varphi}$  represents the derivative of  $\varphi$ .

255 Since nine components of the cross-correlation functions were used in this study,  
 256 we define the following vectors:

$$257 \quad \mathbf{Y}_t \equiv \begin{pmatrix} \mathbf{y}_t^{RR} \\ \mathbf{y}_t^{RT} \\ \mathbf{y}_t^{RZ} \\ \mathbf{y}_t^{TR} \\ \mathbf{y}_t^{TT} \\ \mathbf{y}_t^{TZ} \\ \mathbf{y}_t^{ZR} \\ \mathbf{y}_t^{ZT} \\ \mathbf{y}_t^{ZZ} \end{pmatrix}, \mathbf{Z}_t(\hat{\boldsymbol{\alpha}}_t) \equiv \begin{pmatrix} \boldsymbol{\zeta}_t^{RR} \\ \boldsymbol{\zeta}_t^{RT} \\ \boldsymbol{\zeta}_t^{RZ} \\ \boldsymbol{\zeta}_t^{TR} \\ \boldsymbol{\zeta}_t^{TT} \\ \boldsymbol{\zeta}_t^{TZ} \\ \boldsymbol{\zeta}_t^{ZR} \\ \boldsymbol{\zeta}_t^{ZT} \\ \boldsymbol{\zeta}_t^{ZZ} \end{pmatrix}, \mathbf{M}_t(\hat{\boldsymbol{\alpha}}_t) \equiv \begin{pmatrix} \mathbf{m}^{RR}(\hat{\boldsymbol{\alpha}}_t + \mathbf{R}_t + \mathbf{E}_t) \\ \mathbf{m}^{RT}(\hat{\boldsymbol{\alpha}}_t + \mathbf{R}_t + \mathbf{E}_t) \\ \mathbf{m}^{RZ}(\hat{\boldsymbol{\alpha}}_t + \mathbf{R}_t + \mathbf{E}_t) \\ \mathbf{m}^{TR}(\hat{\boldsymbol{\alpha}}_t + \mathbf{R}_t + \mathbf{E}_t) \\ \mathbf{m}^{TT}(\hat{\boldsymbol{\alpha}}_t + \mathbf{R}_t + \mathbf{E}_t) \\ \mathbf{m}^{TZ}(\hat{\boldsymbol{\alpha}}_t + \mathbf{R}_t + \mathbf{E}_t) \\ \mathbf{m}^{ZR}(\hat{\boldsymbol{\alpha}}_t + \mathbf{R}_t + \mathbf{E}_t) \\ \mathbf{m}^{ZT}(\hat{\boldsymbol{\alpha}}_t + \mathbf{R}_t + \mathbf{E}_t) \\ \mathbf{m}^{ZZ}(\hat{\boldsymbol{\alpha}}_t + \mathbf{R}_t + \mathbf{E}_t) \end{pmatrix} \quad (14)$$

#### 258 4.1 Calculation of the reference CCF

259 First, we estimated the preliminary reference CCF  $\varphi_{ref}^p$  for the  $p$ th component pair  
 260 as,

$$261 \quad \varphi_{ref}^p(\tau) = \frac{1}{n} \sum_{t=1}^n \phi_t^p(\tau). \quad (15)$$

262 With the preliminary reference CCF, preliminary  $\hat{\gamma}_t$  was measured using an extended  
 263 Kalman filter/smoothen described in the following subsections. Then we recalculated the  
 264 reference as

$$265 \quad \varphi_{ref}^p(\tau) = \frac{1}{n} \sum_{t=1}^n \phi_t^p(\tau(1 + \hat{\gamma}_t)). \quad (16)$$

266 After recalculating  $\hat{\gamma}_t$  with the revised reference, we measured the temporal variations  
 267 that are discussed herein.

## 268 4.2 Extended Kalman filter

269 The state vector  $\alpha_t$  was estimated by the recursive linear Kalman (forward) filter  
 270 and (backward) smoother. The Kalman filter/smoothen is a powerful solver of a state-  
 271 space model, which obeys Gaussian distributions (e.g., Durbin & Koopman, 2012). The  
 272 method has been applied for many geophysical problems (e.g. geodetic inversions, Segall  
 273 & Matthews, 1997; Aoki et al., 1999), and recursive travel-time inversion in seismology  
 274 (Ogiso et al., 2005). Since state vectors obey a normal distribution, the means and the  
 275 covariance matrices characterized the statistics of the vector completely. Let us consider  
 276 the conditional mean and covariance matrix of the state variables at time  $t = 2 \dots n$   
 277 for given data through  $\mathbf{Y}_1, \dots, \mathbf{Y}_{t-1}$  as,

$$278 \quad \hat{\alpha}_{t|t-1} \equiv E(\alpha_t | \mathbf{Y}_1, \dots, \mathbf{Y}_{t-1}) \quad (17)$$

$$279 \quad \hat{\mathbf{P}}_{t|t-1} \equiv Cov(\alpha_t | \mathbf{Y}_1, \dots, \mathbf{Y}_{t-1}), \quad (18)$$

281 where  $n$  is number of the data,  $E()$  represents expectation, and  $Cov()$  represents covari-  
 282 ance.  $\hat{\alpha}_{t|t-1}$  is also known as the one-step ahead predictor (Durbin & Koopman, 2012).  
 283 Since no data can constrain  $\hat{\alpha}_{1|0}$  and  $\hat{\mathbf{P}}_{1|0}$ , they are given by the initial values:  $\hat{\alpha}_{1|0} =$   
 284  $\mathbf{a}_1$  and  $\hat{\mathbf{P}}_{1|0} = \mathbf{P}_1$ .

285 These are updated from the initial value  $\mathbf{a}_1$  and  $\mathbf{P}_1$  using the following equation:

$$286 \quad \hat{\alpha}_{t+1|t} = \hat{\alpha}_{t|t-1} + \mathbf{K}_t \mathbf{v}_t \quad (19)$$

$$287 \quad \hat{\mathbf{P}}_{t+1|t} = \hat{\mathbf{P}}_{t|t-1} - \mathbf{K}_t (\mathbf{Z}_t \hat{\mathbf{P}}_{t|t-1} \mathbf{Z}_t^T + \mathbf{H}_t) \mathbf{K}_t^T + \mathbf{Q}_t, \quad (20)$$

289 where Kalman gain  $\mathbf{K}_t$  is given by

$$290 \quad \mathbf{K}_t = \hat{\mathbf{P}}_{t|t-1} \mathbf{Z}_t^T (\mathbf{H}_t + \mathbf{Z}_t \hat{\mathbf{P}}_{t|t-1} \mathbf{Z}_t^T)^{-1}, \quad (21)$$

291 and the innovation vector  $\mathbf{v}_t$  is given by

$$292 \quad \mathbf{v}_t = \mathbf{Y}_t - \mathbf{M}_t(\hat{\alpha}_{t|t-1}). \quad (22)$$

293 Since the number of model parameters of 2 is much smaller than length of  $\mathbf{Y}_t$  of 36000  
 294 (9 components  $\times$  400 points), the matrix calculation of equation (21) can be reduced us-  
 295 ing the following matrix inversion lemma (Tarantola & Valette, 1982; Ogiso et al., 2005),

$$296 \quad (\mathbf{H}_t + \mathbf{Z}_t \hat{\mathbf{P}}_{t|t-1} \mathbf{Z}_t^T)^{-1} = \mathbf{H}_t^{-1} - \mathbf{H}_t^{-1} \mathbf{Z}_t (\hat{\mathbf{P}}_{t|t-1}^{-1} + \mathbf{Z}_t^T \mathbf{H}_t^{-1} \mathbf{Z}_t)^{-1} \mathbf{Z}_t^T \mathbf{H}_t^{-1}. \quad (23)$$

297 Here we assumed that the errors of the CCF are independent of lag time, and the  
 298 variances were the same throughout the lag time. Since we assumed that the covariance  
 299 matrix of data error  $\mathbf{H}_t$  is represented by  $\mathbf{H}_t = h_0 \mathbf{I}$  (equation (8)), the forward recur-  
 300 sive equations (19) and (20) could be simplified as,

$$301 \quad \hat{\alpha}_{t+1|t} = \hat{\alpha}_{t|t-1} + \Xi_t \Gamma_t \quad (24)$$

$$302 \quad \hat{\mathbf{P}}_{t+1|t} = \hat{\mathbf{P}}_{t|t-1} - \Xi_t (\mathbf{S}_t \hat{\mathbf{P}}_{t|t-1} \mathbf{S}_t + h_0 \mathbf{S}_t) \Xi_t^T + \mathbf{Q}_t, \quad (25)$$

where  $\mathbf{S}_t$  and  $\mathbf{\Xi}_t$  are  $2 \times 2$  matrices as:

$$\mathbf{S}_t \equiv \sum_p (\zeta_t^p)^T \zeta_t^p, \quad (26)$$

$$\mathbf{\Gamma}_t \equiv \sum_p (\zeta_t^p)^T \mathbf{v}_t^p, \quad (27)$$

$$\mathbf{\Xi}_t \equiv \left( \frac{1}{h_0} \hat{\mathbf{P}}_{t|t-1} - \frac{1}{h_0^2} \hat{\mathbf{P}}_{t|t-1} \mathbf{S}_t \left( \frac{\mathbf{S}_t}{h_0} + \hat{\mathbf{P}}_{t|t-1}^{-1} \right)^{-1} \right). \quad (28)$$

### 4.3 Kalman smoother

Next, let us consider the conditional mean  $\hat{\alpha}_{t|n}$  and conditional covariance matrix  $\hat{\mathbf{P}}_{t|n}$  of the state variables at time  $t$  for all data through  $\mathbf{Y}_1, \dots, \mathbf{Y}_n$ . With the  $\hat{\alpha}_{t|t-1}$  and  $\hat{\mathbf{P}}_{t|t-1}$  ( $t = 2, \dots, n$ ) estimated in the previous subsection, they can be calculated by the following backward recursive equations,

$$\hat{\alpha}_{t|n} = \hat{\alpha}_{t|t-1} + \hat{\mathbf{A}}_t (\hat{\alpha}_{t+1|n} - \hat{\alpha}_{t|t-1}), \quad (29)$$

$$\hat{\mathbf{P}}_{t|n} = \hat{\mathbf{P}}_{t+1|t} - \mathbf{Q}_t + \hat{\mathbf{A}}_t (\hat{\mathbf{P}}_{t+1|n} - \hat{\mathbf{P}}_{t+1|t}) \hat{\mathbf{A}}_t^T. \quad (30)$$

where  $\mathbf{A}_t$  is defined by

$$\hat{\mathbf{A}}_t = \left( \mathbf{I} - \mathbf{Q}_t \hat{\mathbf{P}}_{t+1|t}^{-1} \right), \quad (31)$$

The recursive equations were applied successively backward as  $t = n - 1, \dots, 1$ .

### 4.4 Temporal change of seismic wave velocity

First, we tentatively estimated the temporal variations without the explanatory variables. For given hyper-parameters  $r_t = e_t = 0$ ,  $p_0 = 5 \times 10^{-4}$ ,  $p_1 = 5 \times 10^{-5}$ , we estimated the state variables using the extended Kalman filter/smoothen. Figure 4 shows the result of temporal variations in seismic velocity  $\hat{\gamma}_{t|n}$  and the corresponding standard deviation by applying CCFs of the station pair between TKW and TKS. The figure shows clear seasonal variation, and the velocity drops coincide with strong rainfalls (blue bars in the figure). The red line shows the precipitation model (see the next section for details). This figure also shows a sudden velocity drop of about 0.1 % when the Kumamoto earthquake occurred in 2016. To detect signals associated with volcanic eruptions, we subtracted the precipitation effects and the earthquake drop from the temporal variations in seismic velocity. For the subtraction, we infer the hyper-parameters, which represent the model covariances, precipitation effects, and earthquake, drop by the Maximum Likelihood method in the next section.

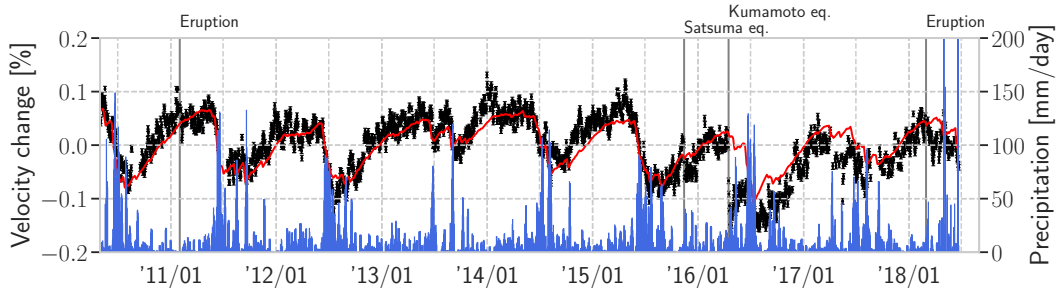


**Figure 4.** Row temporal changes of the pair between TKW and TKS with the prediction from the precipitation. The red line shows prediction by the precipitation model ( $\tau_g = 195$  days, and  $A_g = -6.84 \times 10^{-2}$  [%/m]), as described in the next section.

## 5 Maximum Likelihood Method for determining the hyper-parameters

In the previous section, we applied the extended Kalman filter/smoothen, assuming that the hyper-parameters were given at the lower level. This section shows how to infer the hyper-parameters using the Maximum Likelihood Method at the higher level of this technique.

The logarithmic likelihood  $\ln L$  is given (e.g., Segall & Matthews, 1997; Durbin & Koopman, 2012) by

$$\ln L = -\frac{nN}{2} \ln 2\pi - \frac{1}{2} \sum_{t=1}^n \left( \ln(\det(\mathbf{F}_t)) + \hat{\mathbf{d}}_{t|t-1} \right), \quad (32)$$

where  $\mathbf{F}_t$  and  $\hat{\mathbf{d}}_{t|t-1}$  are given by,

$$\mathbf{F}_t \equiv h_0 \mathbf{I} + \mathbf{Z}_t \hat{\mathbf{P}}_{t|t-1} \mathbf{Z}_t^T, \quad (33)$$

and

$$\hat{\mathbf{d}}_{t|t-1} = \frac{1}{h_0^2} \left( h_0 \mathbf{v}_t^T \mathbf{v}_t - \mathbf{\Gamma}_t^T \left( \hat{\mathbf{P}}_{t|t-1}^{-1} + \frac{\mathbf{S}_t}{h_0} \right)^{-1} \right) \mathbf{\Gamma}_t, \quad (34)$$

respectively. We maximized the logarithmic likelihood  $\ln L$  with respect to the hyper-parameters.

First, we describe how to model the hyper-parameters for explaining the precipitation effects and the reduction associated with the 2016 Kumamoto earthquake in the following two subsections.

### 5.1 A model for the precipitation effects

Many researchers have reported periodic changes in seismic wave velocity associated with external sources such as tides (e.g., Yamamura et al., 2003; Takano et al., 2014, 2019), thermoelastic effects (e.g., Hillers, Ben-Zion, et al., 2015; Wang et al., 2017), and snow loading (e.g., Wang et al., 2017). The correspondence between strong rainfall and the seismic velocity changes shown in Figure 4 suggests the dominance of the precipitation effect in this case. For modeling temporal changes of seismic wave velocity caused by precipitation, we considered two models: the model based on diffusion of a pore pressure (Talwani et al., 2007; Rivet et al., 2015; Lecocq et al., 2017; Wang et al., 2017), and the hydrological model (Sens-Schönfelder & Wegler, 2006).

The first model considered diffusion of pore pressure in a poroelastic medium with a spatial scale of several km, which induces seismic velocity changes. This model also required the sensitivity of seismic velocity to changes in pore pressure. As discussed in section 7.2, the sensitivity is an order of magnitude smaller than the typical values. The diffusion of pore pressure also caused significant time delay, which is not consistent with the observations in this study.

The second model related the seismic velocity to the groundwater level at a shallow depth due to the precipitation (Sens-Schönfelder & Wegler, 2006). Since the groundwater level reaches a shallow depth of about 100 m in this region (Kagiyama et al., 1996; Tsukamoto et al., 2018), we regarded the second model more relevant. The response of the groundwater level to the precipitation is given by an exponential function (Sens-Schönfelder & Wegler, 2006; Kim & Lekic, 2019). The amount of ground water storage  $g_t$  is given by

$$g_t = \int_t^\infty (p(\tau) - \langle p \rangle) e^{-\frac{t-(\tau+\delta)}{\tau_g}} d\tau, \quad (35)$$

where  $p$  is daily precipitation,  $\delta$  shows delay time,  $\tau_g$  is the parameter describing the decay,  $\langle p \rangle$  is the average precipitation throughout the analyzed time period. We modeled

377 that the explanatory variable for precipitation  $r_t$  is proportional to  $g_t$  as,

$$378 \quad r_t = A_g g_t = A_g \int_t^\infty (p(\tau) - \langle p \rangle) e^{-\frac{t-(\tau+\delta)}{\tau_g}} d\tau, \quad (36)$$

379 where  $A_g$  is the sensitivity of seismic wave velocity to the ground water level. Since there  
 380 exists ambiguity of the modeling,  $A_g$ ,  $\tau_g$ , and  $\delta$  should be constrained by the observa-  
 381 tions practically. We regard  $A_g$ ,  $\tau_g$  and  $\delta$  as hyper-parameters, and infer their values by  
 382 the Maximum Likelihood Method as shown later in this section.

383 To validate the second model quantitatively, we estimate the sensitivity  $A_g$  based  
 384 on a physical model: density perturbation due to groundwater levels causes the tempo-  
 385 ral change associated with precipitation. Since surface waves are dominant in the wave-  
 386 field in this frequency range, the depth sensitivity can be represented by that of the sur-  
 387 face waves for a 1-D medium (Obermann et al., 2013). We consider only Rayleigh waves  
 388 for simplicity, since a similar discussion can be applicable for Love waves. The phase ve-  
 389 locity perturbation of Rayleigh waves  $\delta c$  can be related to perturbations of density  $\rho$ ,  
 390 bulk modulus  $\kappa$ , and andrigidity  $\mu$  using the partial derivatives of phase velocity (Takeuchi  
 391 & Saito, 1972) as,

$$392 \quad \frac{\delta c}{c} = \int \left( K_\rho(z) \frac{\delta \rho(z)}{\rho(z)} + K_\kappa(z) \frac{\delta \kappa(z)}{\kappa(z)} + K_\mu(z) \frac{\delta \mu(z)}{\mu(z)} \right) dz, \quad (37)$$

393 where  $c$  is the phase velocity, and  $K_\rho$ ,  $K_\kappa$  and  $K_\mu$  are the Fréchet derivatives relating  
 394 the fractional perturbation of phase velocity  $\delta c/c$  to the fractional perturbations  $\delta \rho/\rho$ ,  
 395  $\delta \kappa/\kappa$ ,  $\delta \mu/\mu$ . The Fréchet derivatives are also known as the depth sensitivity kernels. Fig-  
 396 ure 5 shows an example of a depth sensitivity kernel at 0.6 Hz for the density and S-wave  
 397 velocity models shown in the figure.

398 Working under the two assumption of (i) no temporal changes in bulk modulus  $\kappa$   
 399 and the rigidity  $\mu$ , and (ii) the groundwater level of about 100 m, the temporal change  
 400  $r_t$  can be estimated as,

$$401 \quad r_t = \int K_\rho(z) \frac{\delta \rho(z)}{\rho(z)} dz \approx K_\rho(0) \frac{\rho_w g_t}{\rho(0)}, \quad (38)$$

402 where  $\rho_w$  is water density. Accordingly,  $A_g$  can be written by  $K_\rho(0) \frac{\rho_w}{\rho(0)}$ . For example,  
 403 with the model shown by Figure 5,  $A_g$  is estimated to be  $-7.5 \times 10^{-2}$  [%/m]. The con-  
 404 sistency between this estimate of  $-7.5 \times 10^{-2}$  [%/m] and the fitting result of  $-6.84 \times$   
 405  $10^{-2}$  [%/m] supports our model.

406 For estimation of the hyper-parameters, initial values are required. We estimated  
 407 them in two steps. First, using the preliminary reference CCF,  $\hat{\gamma}_{t|n}$  was calculated for  
 408 each station pair. In equation (5),  $\mathbf{R}_t$  is assumed to be  $\mathbf{0}$ . Then,  $A_g$  and  $\tau_g$  were esti-  
 409 mated by calculating the least squared difference between  $r_t$  and  $\hat{\gamma}_{t|n}$ .  $\delta$  is fixed to 0. The  
 410 red line in Figure 4 shows the initial estimate of a pair between TKW and TKS:  $\tau_g =$   
 411  $195$  days and  $A_g = -6.84 \times 10^2$  [%/m]. This figure shows that the empirical model  
 412 can predict the seasonal variations well. To avoid the effects of the sudden drop due to  
 413 the 2016 Kumamoto earthquake, we used the data from before the earthquake in the es-  
 414 timation.

## 415 5.2 A model for the drops associated with 2016 Kumamoto earthquake

416 After the reduction of the effect of precipitation with the tentative hyper-parameters,  
 417 the resultant temporal change shows sudden drops of seismic wave velocity associated  
 418 with the 2016 Kumamoto earthquake (Figure 6). Since the drop related to the Kumamoto  
 419 earthquake reaches 0.1 %, we modeled it by an exponential decay (Hobiger et al., 2016;  
 420 Gassenmeier et al., 2016; Sens-Schönfelder & Eulenfeld, 2019) as,

$$421 \quad e_t = A_t e^{-\frac{t-t_0}{\tau_e}}, \quad (39)$$

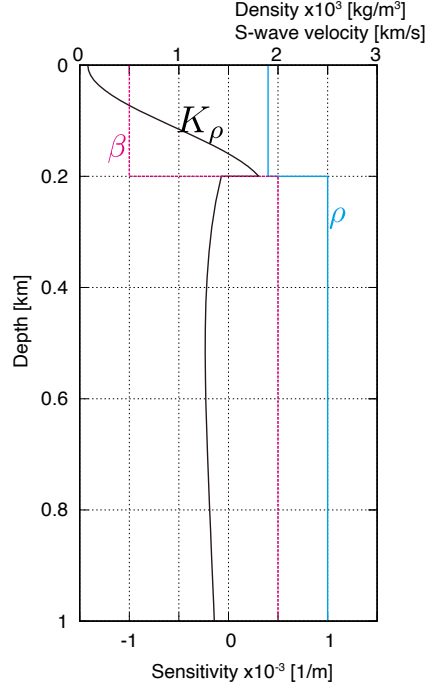


**Figure 5.** Depth sensitivity kernel to density perturbations at 0.6 Hz. The density  $\rho$  and the S-wave velocity  $\beta$  are plotted. P-wave velocities are 1.91 km/s from 0 to 0.2 km, and 4 km/s below 0.2 km.

422 where  $A_t$  is amplitude of the drop,  $t_0$  is the origin time of the Kumamoto earthquake,  
 423 and  $\tau_e$  is the decay time. We omitted a term of non-recovering coseismic velocity drops  
 424 (Hobiger et al., 2016) as the term could not be detected, as shown later (see Figure 10).

### 425 **5.3 Estimation of the hyper-parameters by Maximum Likelihood Method**

426 To reduce the number of hyper-parameters, we assumed that the expected value  
 427 of the initial state variable  $\mathbf{a}_1$  is given by  $(1, \gamma_1)$ , and the covariance matrix  $\mathbf{P}_1$  is equal  
 428 to  $\mathbf{Q}_t$ .

429  $\ln L$  is a function of hyper-parameters  $\beta$ , where

$$430 \quad \beta = (p_0, p_1, \tau_g, A_g, \delta, \gamma_1, A_e, \tau_e). \quad (40)$$

431 The logarithmic likelihood  $\ln L$  was maximized with respect to the hyper-parameters us-  
 432 ing a quasi-Newton method L-BFGS-B, which is a limited memory algorithm for solv-  
 433 ing large nonlinear optimization problems subject to simple bounds on the variables (Zhu  
 434 et al., 1994; Durbin & Koopman, 2012).

435 Figure 7 shows estimated hyper-parameters, which are well constrained by the ob-  
 436 servations. Figure 7 (a) shows the model standard deviations of amplitude  $A_t$  of about  
 437  $5 \times 10^3 \%$  and those of stretching factor  $\gamma_t$  of about 0.1%. We note that the observed  
 438 data constrain the model standard deviations. Figure 7 (b) shows a trend of decreas-  
 439 ing sensitivity  $A_g$  with decreasing decay time  $\tau_g$ . This result suggests that the ground-  
 440 water level changes at shallower depths have shorter time decay time  $\tau_g$ , because the depth  
 441 sensitivity kernel is negative and decreases to the ground surface (Figure 5). Figure 7  
 442 (c), which compares  $A_e$  and  $\tau_e$ , shows the drop when the earthquake becomes larger, de-

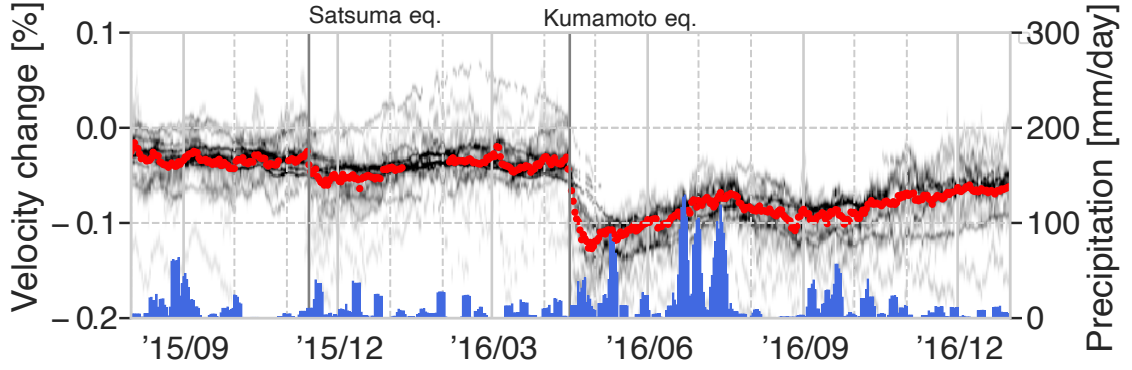


**Figure 6.** Velocity change associated with the 2016 Kumamoto earthquake. The seismic velocity drop when the earthquake occurred, and recovered over a time scale of three months. The grayscale shows marginal probability with all CCFs (see next section for details). The red dots show a median of all the measurements. The red dots also show a minor drop during the 2015 Satsuma earthquake.

443 creasing the recovery time. This result suggests that the stronger drop and shorter re-  
 444 recovery occurred at shallower depths.

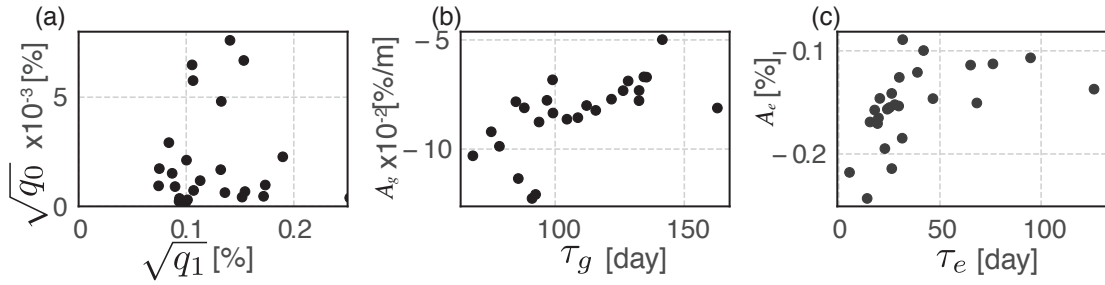


**Figure 7.** Estimated hyper-parameters. (a) scatter plot against standard deviations of the model:  $\sqrt{q_0}$  and  $\sqrt{q_1}$ , (b) scatter plot against hyper-parameters of precipitation effects:  $\tau_g$  and  $A_g$ , (c) scatter plot against hyper-parameters of the drop during the Kumamoto earthquake:  $A_e$  and  $\tau_e$ .

445 To determine how well the observations constrain the hyper-parameters  $\beta$ , we esti-  
 446 mated the sensitivity of the logarithmic likelihood of the perturbations around the op-  
 447 timal value  $\beta^{opt}$ . Figure 8 shows an increment of logarithmic likelihood to the opti-  
 448 mal value of  $\Delta \ln L$  as a function of a hyper-parameter. We perturbed each hyper-parameter  
 449 within 50%, fixing all other hyper-parameters to the optimal values. Within this hyper-  
 450 parameter range, the minima of  $\Delta \ln L$  for all the hyper-parameters were smaller than  
 451 -1.

452 Here we considered the appropriate number of hyper-parameters using the Akaike  
 453 Information Criterion ( $AIC$ , Akaike, 1974) defined by

$$454 \quad AIC_K = -2 \ln \hat{L}_K + 2K, \quad (41)$$

455 where  $K$  is the number of hyper-parameters, and  $\ln \hat{L}_K$  represents the maximum like-  
 456 lihood for the  $K$  hyper-parameters. We choose the hyper-parameter if  $AIC_K$  decreases

457 with the addition of a new hyper-parameter: i.e. the increment  $\Delta AIC \equiv AIC_K - AIC_{K-1}$   
 458 is smaller than 0. Assuming that  $\ln \hat{L}_{K-1} - \ln \hat{L}_K$  can be approximated by  $\Delta \ln L$  shown  
 459 in Figure 8, the  $\Delta AIC$  is written by  $2(\Delta \ln L + 1)$ . The addition of a hyper-parameter  
 460 is appropriate if  $\Delta \ln L < -1$ . Assuming that the ambiguity of each parameter is about  
 461 50%, for example,  $\beta_i$  is fixed at  $0.5\beta_i^{opt}$  as the prior value. Since all the  $\Delta \ln L$  at  $\beta_i/\beta_i^{opt} =$   
 462 0.5 in Figure 8 are smaller than  $-1$ , all the hyper-parameters used meet this condition.  
 463 This choice of hyper-parameters also makes the iterations of the L-BFGS-B method stable.  
 464

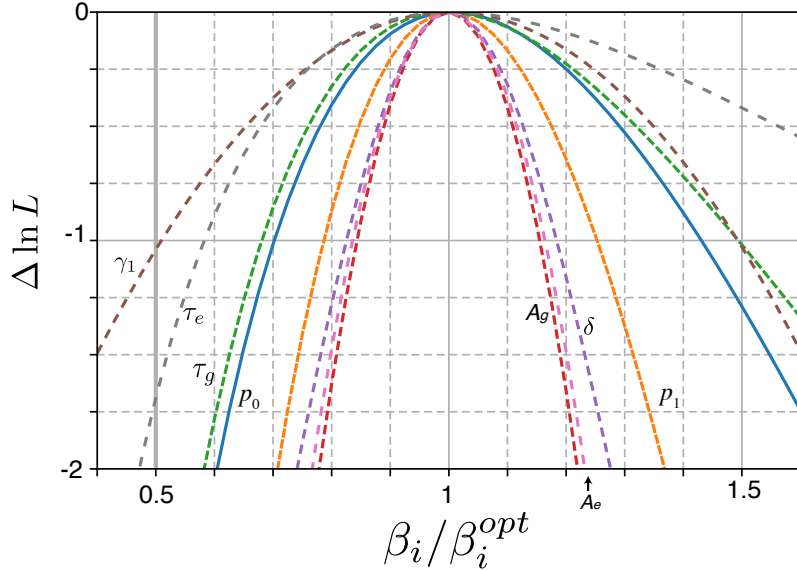


**Figure 8.** Logarithmic likelihood as a function of the normalized hyper-parameters. The horizontal axis shows relative value of hyper-parameters, and the vertical axis shows increments of logarithmic likelihood to the optimal value  $\ln L(\beta^{opt})$ . The corresponding hyper-parameters ( $\beta_i$ ) are also shown in this figure.

## 6 Temporal changes of seismic wave velocity

465

466

467

468

469

470

Using the inferred hyper-parameters, we estimated state variables for all pairs of stations. Red lines in the upper triangular portion of Figure 9 show the total temporal changes of seismic wave velocity  $\hat{\gamma}_{t|n} + r_t + e_t$ . The blue lines show only the explanatory variables  $r_t + e_t$  for precipitation and the earthquake. The explanatory variables can explain majority of the aspects of the estimated temporal changes.

471

472

473

474

475

476

477

478

479

480

The lower triangular portion of Figure 9 shows the resultant  $\hat{\alpha}_{t|n}$ . The blue lines show the amplitude  $\hat{A}_{t|n}$ , which show the local minimum in 2015. High activities of low-frequency volcanic tremor at Mt. Aso (Figure 1) could distort the coherency (Kaneshima et al., 1996; Hendriyana & Tsuji, 2019; Sandanbata et al., 2015). The red lines show seismic velocity changes,  $\hat{\gamma}_{t|n}$ , after the subtraction of the explanatory variables. They show a consistent long term variation with a time scale of about five years with an amplitude of about 0.05 %. Although most station pairs do not show significant temporal changes associated with the 2011 eruption, the pair between SMW and SMN shows a significant drop in 2011. The upper triangular portion shows the precipitation effect and the drop associated with the earthquake are well subtracted using the explanatory variables.

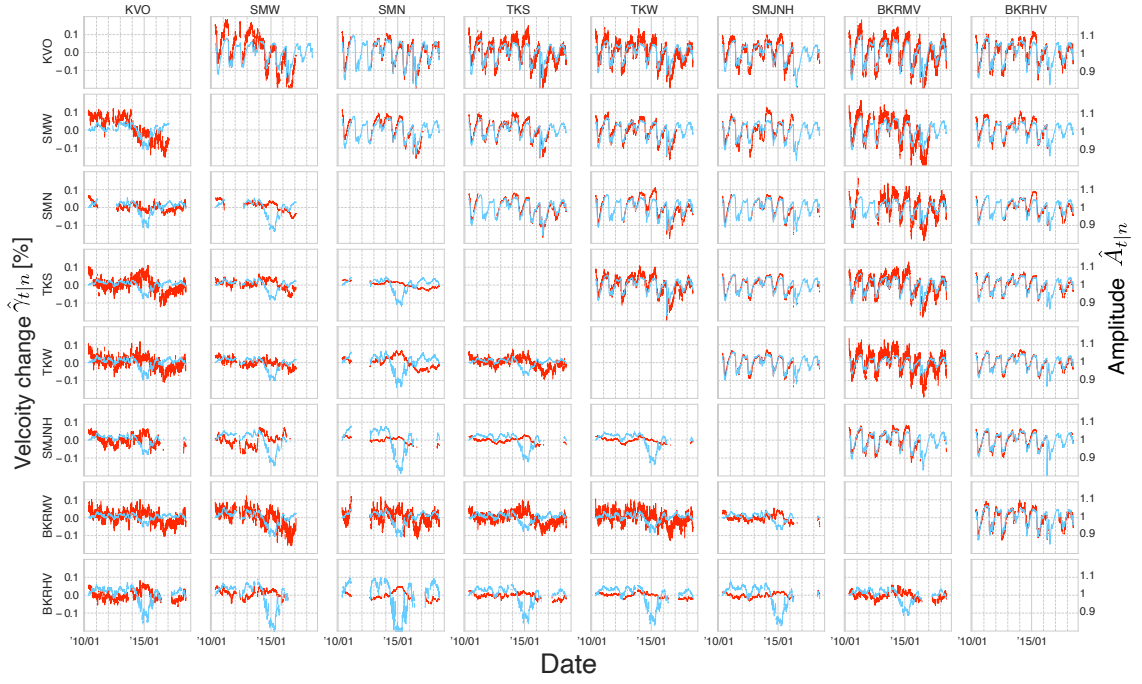


**Figure 9.** The lower triangular portion: resultant  $\hat{\alpha}_{t|n}$ . The red lines show seismic velocity change  $\hat{\gamma}_{t|n}$  within 0.1%. The blue lines show the amplitude perturbations  $\hat{A}_{t|n}$ , which show a local minimum in 2015. The upper triangular portion: Blue lines show estimated seismic velocity changes  $r_t + e_t$ , which explain the precipitation effect and the drop during the Kumamoto earthquake, whereas red ones show estimated whole seismic velocity changes  $\hat{\gamma}_{t|n} + r_t + e_t$ .

481 To discuss the long-term variations, we considered the marginal probability den-  
 482 sity with all pairs of stations. Figure 10(a) shows the marginal probability density over  
 483 8 years with an assumption that each measurement is independent. The probability den-  
 484 sity  $f_t(\gamma)$  as a function of seismic velocity change  $\gamma$  is defined by

$$485 \quad f_t(\gamma) \equiv \frac{1}{28} \sum_{j=1}^{28} \mathcal{N}(^j\hat{\gamma}_{t|n}, ^j\hat{q}_{t|n}), \quad (42)$$

486 where  $\mathcal{N}$  represents normal distribution,  $^j\hat{\gamma}_{t|n}$  is the conditional mean of seismic veloc-  
 487 ity changes,  $^j\hat{q}_{t|n}$  is the corresponding conditional covariance,  $j$  indicates a station pair,  
 488 and 28 is the total number of station pairs. The marginal probability density (Figure  
 489 10(a)) shows no significant changes associated with the 2011 and 2018 eruptions of Shinmoe-  
 490 dake. However, areal strain calculated from GNSS observation shows inflation and de-  
 491 flation due to changes in the magma reservoir during the 2011 eruption, and the 2018  
 492 eruption (Nakao et al., 2013; Kozono et al., 2013; Yamada et al., 2019) (Figure 10(b)).  
 493 The areal strain also shows the static change due to the 2016 Kumamoto earthquake,  
 494 whereas  $f_t(\gamma)$  does not show significant static change.

495 Apart from jumps of the areal strain associated with the eruptions and the earth-  
 496 quake, both the seismic velocity changes and the areal strain (Figure 10) show tempo-  
 497 ral variations with a time scale of about one year with local maxima in January 2012 and  
 498 January 2013. After 2014, such temporal variations are no longer observed for both. One  
 499 possible origin of the variations is the long term variations in groundwater levels (e.g.,  
 500 Lecocq et al., 2017). When modeling groundwater level in equation (35), we assumed  
 501 constant drainage. Nevertheless, under realistic conditions, the drainage may change with  
 502 time. Since the areal strain also shows a similar undulation pattern from 2010 to 2013,  
 503 such a long-term variation may cause large scale deformations. The induced pore pres-  
 504 sure change (Talwani et al., 2007) at deeper depth, on the order of km, could also cause  
 505 seismic velocity changes (Wang et al., 2017; Rivet et al., 2015). In this study, however,  
 506 the hydrological data were insufficient to verify this hypothesis.

## 507 7 Discussions

508 In the following subsections, we discuss two specific events: the drop of seismic wave  
 509 velocity associated with the Kumamoto earthquake and the 2011 Shinmoe-dake erup-  
 510 tion. Based on the observed features, we discuss the magma pathway beneath Shinmoe-  
 511 dake.

### 512 7.1 The drop of seismic wave velocity after the Kumamoto earthquake

513 Our results show a sudden drop during the Kumamoto earthquake followed by a  
 514 recovery from 10 to 100 days (Figure 7). Since the probability density  $f_t(\gamma)$  does not show  
 515 non-recovering coseismic velocity drops due to the static areal-strain change (Figure 10),  
 516 the observed static strain change could not be the dominant source. Near-surface dam-  
 517 age beyond the linear elastic regime could be a possible origin. For the discussion, we  
 518 compare the susceptibility, which is defined by the ratio between observed reductions in  
 519 seismic velocity and the estimated dynamic stress with that of the 2011 Tohoku earth-  
 520 quake (Brenugier et al., 2014).

521 We estimated the dynamic stress from the observed peak ground velocity (PGV)  
 522 (Gomberg & Agnew, 1996). PGV in this region was about 5 cm/s during the Kumamoto  
 523 earthquake, which was averaged over 3 components of PGV measured by the K-net, strong-  
 524 motion seismograph network. The dynamic stress  $\Delta\sigma \approx \mu v/c$  was estimated to be 0.5 MPa,  
 525 where  $\mu$  is the mean crustal shear modulus ( $\sim 30$  GPa),  $v$  is PGV, and  $c$  is the mean  
 526 wave phase velocity of the Rayleigh wave ( $\sim 3$  km/s) (Brenugier et al., 2014). The sus-  
 527 ceptibility (Brenugier et al., 2014), which is defined by the ratio between observed re-

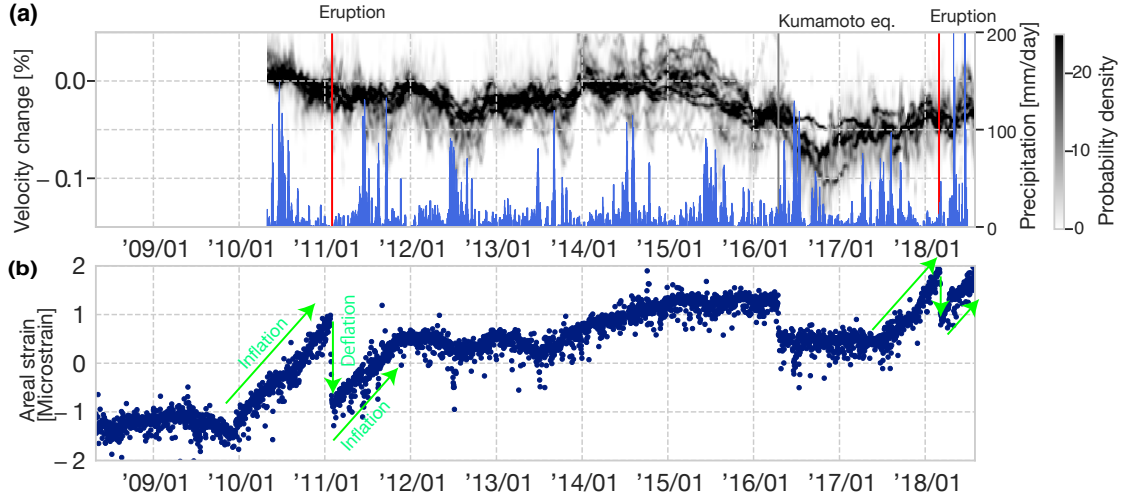


**Figure 10.** (a) Marginal probability density of all pairs of stations. The blue bars show daily precipitation data at the JMA meteorological station. The estimated seismic velocities scatter from Oct. 2014 to May 2015 when the activity of low frequency tremor at Mt. Aso occurs. (b) Areal strain calculated from three GEONET stations: Ebino, Miyakonojou2 and Makizono shown in Figure 1.

528 reductions in seismic velocity  $\Delta c/c$  ( $\sim 2 \times 10^{-3}$ ) and the estimated dynamic stress 0.5 MPa,  
 529 was about  $4 \times 10^{-3} \text{ MPa}^{-1}$ . This value is larger than susceptibility in the Mt. Fuji area  
 530 and along the Tohoku volcanic during the Tohoku earthquake, whose value is about  $1.5 \times$   
 531  $10^{-3} \text{ MPa}^{-1}$  (Brenquier et al., 2014). This observation suggests that the pressurized ge-  
 532 offluid in the upper crust and/or near-surface is a possible origin for the seismic veloci-  
 533 ty changes.

534 We discuss the mechanism of the observed seismic velocity change as caused by the  
 535 pressurized fluid. The exponential decay time scales ranged from 10 to 100 days, sug-  
 536 gesting the lack of a relaxation process longer than 100 days (Snieder et al., 2017). The  
 537 estimation of relatively short time scales dismisses the mechanisms of post-seismic re-  
 538 laxation of stress (e.g., Brenquier, Shapiro, et al., 2008) and diffusion of geofluid in the  
 539 crust (Wang et al., 2019). The absence of non-recovering coseismic velocity drop dur-  
 540 ing the 2016 Kumamoto earthquake suggests that the pressurization of geofluid in the  
 541 linear elastic regime is unlikely to be the origin. This hypothesis is also consistent with  
 542 the observation that the 2011 Tohoku earthquake did not trigger any volcanic and seis-  
 543 mic activities in this region (Miyazawa, 2011). Near-surface damage due to the strong  
 544 ground motions beyond the linear elastic regime, where rich groundwater exists, could  
 545 be a plausible origin.

546 **7.2 Temporal changes during the volcanic eruptions in 2011**

547 The probability density of all the station pairs  $f_t$  (Figure 10(a)) does not show any  
 548 temporal change associated with the volcanic eruptions from January 2011 to February  
 549 2011. However, geodetic observation showed the gradual magma intrusion over the time  
 550 scale of a year and the discharge during the eruption (see the areal strain in Figure 10(b)).  
 551 The geodetic source was located 5 km to the northwest of the summit at a depth of about  
 552 8 km (Nakao et al., 2013). Although the volumetric change caused enough strain (about

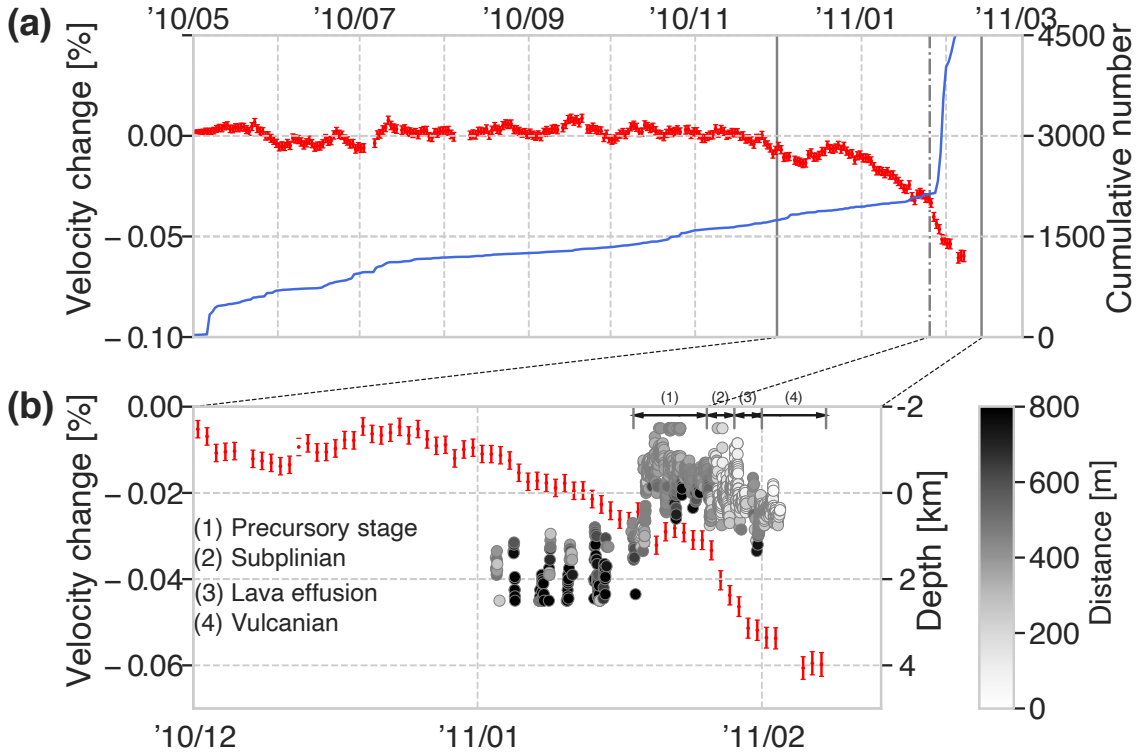


**Figure 11.** (a) Seismic velocity changes  $\hat{\gamma}_{t_n}$  for the pair between SMN and SMW shown by red bars. The station SMN was damaged during the eruption. The line in sky blue shows the cumulative number of volcanic earthquakes determined by JMA below Shinmoe-dake. (b) Enlarged figure from October 1st, 2010 to February 14th, 2011. The panel also shows the depth of volcanic tremor (Ichihara & Matsumoto, 2017). The color of a circle shows the horizontal distance from the center of the summit to the hypocenter. Four periods: (1) Precursory stage, (2) Sub-Plinian, (3) Lava effusion, and (4) Vulcanian (e.g., Nakada et al., 2013; Kozono et al., 2013) are also shown.

553 1.5 microstrains estimated from GNSS as shown by Figure 10) to cause the seismic velocity change with a typical sensitivity of seismic velocity change in a linear elastic regime  
 554 (e.g., Takano et al., 2017), as discussed later, our results do not show a significant change.  
 555 These observations could provide a clue for inferring the state of the material in the upper crust.  
 556  
 557

558 Despite of the absence of observed temporal changes for most station pairs during the 2011 eruption (Figure 9), one station pair close to the crater (SMW and SMN)  
 559 showed a significant drop of seismic velocity (red lines in Figure 11). Figure 11 shows the resultant temporal variations between the station pair (SMW and SMN) from May  
 560 2010 to May 2011. The gradual drop of seismic velocity that preceded the eruption by one month. Since the station SMN was broken 10 days after the main phase of the 2011  
 561 eruption, the post-eruption recovery cannot be discussed.  
 562  
 563  
 564

We discuss the 2011 Shimoedake-eruption based on the two observed temporal variations in seismic wave velocity: (i) no observed temporal variations with the one-year inflation of the magma reservoir, (ii) only the station pair close to the crater detected the gradual decrease preceding the eruption by one month.

First, we consider why the observation only shows temporal variation at one pair. Figure 12 shows areal strain, induced by the point volumetric source, by deflation caused by the migration of magma to the surface. The volumetric source modeled by Nakao et al. (2013) was located at a point (longitude 130.831°E, latitude 31.942°N, depth 8.35 km), which is about 6.9 km northwestern to Shinmoe-dake. The modeled volume change of the deflation is  $13.35 \times 10^6 \text{ m}^3$ . This model can explain the GNSS observations during the deflation in 2011: i.e., this model can explain the observed drop of areal strain based on GNSS shown by Figure 10(b).

The typical areal strain at a depth of 3 km above the volumetric source is  $5 \times 10^{-6}$ , and the typical value of the bulk modulus at a depth of 3 km is 30 GPa. Since the corresponding stress change is  $1.5 \times 10^5 \text{ Pa}$ , the stress sensitivity of seismic velocity change is estimated to be less than  $6 \times 10^{-10} \text{ Pa}^{-1}$ . As this estimated stress sensitivity is an order of magnitude smaller than the past studies at this depth (Takano et al., 2017), our results suggest that the crustal material has lower sensitivity to static stress changes in a linear elastic regime than other regions. This observation is also consistent with that the 2016 Kumamoto earthquake caused only recovering coseismic velocity drops due to dynamic stress but no permanent ones in response to static changes in areal strain (Figure 10). The observed lack of sensitivity is also consistent with our model of precipitation effects, which does not require stress sensitivity of the seismic velocity.

One possible interpretation of the observed low sensitivity or lack of sensitivity could be related to the aspect ratio of crack and/or fluid inclusion of the medium. The low sensitivity suggests that the shape of cracks could be circular (Shapiro, 2003). The P-wave velocity at 3 km is about 5.5 km/s (Tomatsu et al., 2001), and the S-wave velocity is approximately 3.1 km/s (Nagaoka, 2020), suggesting that fraction of the geofluid and crack density should be small. The inclusions of the geofluid could also be isolated because the 3-D inversion of the anomalous magnetotelluric data in this region showed a highly resistive body above the volumetric source (Aizawa et al., 2014).

Next, we considered the spatial localization of the gradual decrease near the crater precedes the eruption by one month. For simplicity, we considered the homogeneous medium with seismic velocity  $c$  of 2 km/s, which correspond to a typical group velocity of Rayleigh waves. We evaluated the sensitivity kernel of the travel time from a point  $\mathbf{s}_1$  to a point  $\mathbf{s}_2$  for local changes of seismic velocities as

$$\left. \frac{\delta c(t)}{c} \right|_{app} = \frac{1}{ct} \int_S K(\mathbf{s}_1, \mathbf{s}_2, \mathbf{r}, t) \delta v(\mathbf{r}) dS(\mathbf{r}), \quad (43)$$

where  $\left. \frac{\delta c(t)}{c} \right|_{app}$  is the apparent velocity change, which corresponds to the measurement,  $t$  is travel time,  $\delta v(\mathbf{r})$  is the perturbation of the seismic velocity at a point  $\mathbf{r}$ ,  $S$  represents the whole surface area, and  $K$  is a sensitivity kernel (Pacheco & Snieder, 2005) given by,

$$K(\mathbf{s}_1, \mathbf{s}_2, \mathbf{r}, t) = \frac{\int_0^t p(\mathbf{s}_1, \mathbf{r}, t') p(\mathbf{r}, \mathbf{s}_2, t - t') dt'}{p(\mathbf{s}_1, \mathbf{s}_2, t)}, \quad (44)$$

where  $p(\mathbf{s}_1, \mathbf{s}_2, t)$  is the probability density that the wave traveled from  $\mathbf{s}_1$  to  $\mathbf{s}_2$  during time  $t$  (Machacca et al., 2019): i.e.  $p(\mathbf{s}_1, \mathbf{r}, t)$  satisfies the normalization condition given by,

$$\int_S p(\mathbf{s}_1, \mathbf{r}, t) dS(\mathbf{r}) = 1. \quad (45)$$

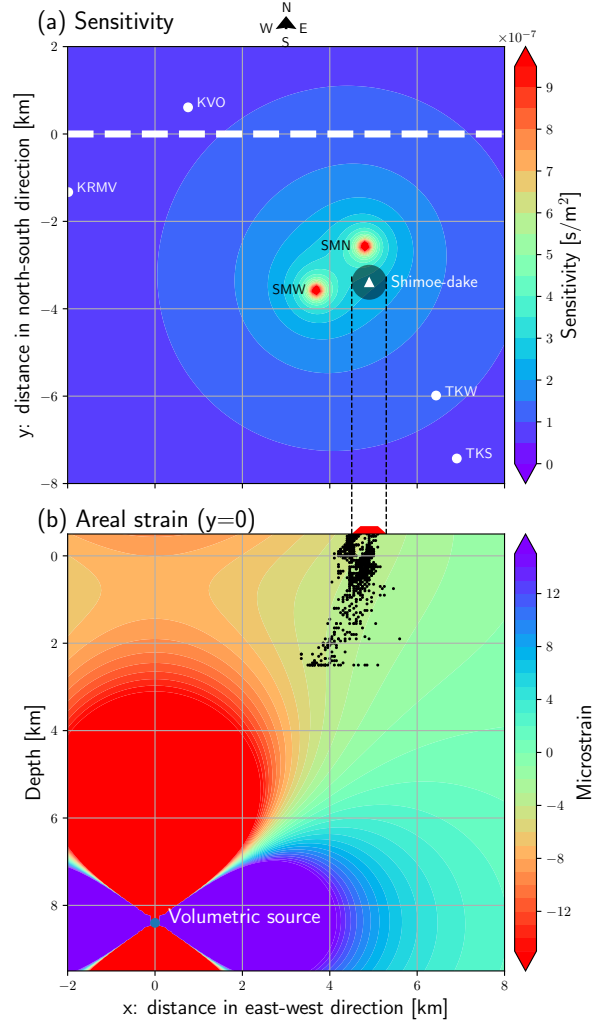


**Figure 12.** (a) Sensitivity kernel (Pacheco & Snieder, 2005; Obermann et al., 2013) at lapse time of 60 s. The scattering mean free path is assumed to be 5000 m. (b): Areal strain induced by the point volumetric source. The model (Nakao et al., 2013) is based on geodetic observation. This panel also shows hypocenters of volcanic tremors given by Ichihara and Matsumoto (2017). Although the hypocenters below 1 km were shifted in a westward direction, the shift might be caused by limited station coverage. We calculated the strain caused by the volumetric source using an inflation point source model (Okada, 1992) in a 3D elastic half-space with a rigidity of 10 GPa, and Poisson’s ratio of 0.25. For simplicity, we assumed that the height of the surface in this area is fixed to 0.5 km above sea level.

611 Here  $p$  is given in the analytic form of the radiative transfer for isotropic scattering in  
 612 2-D (Obermann et al., 2013) as,

$$613 \quad p(r, t) = \frac{\exp\left(-\frac{ct}{l}\right)}{2\pi r} \delta(ct-r) + \frac{1}{2\pi lct} \left(1 - \frac{r^2}{c^2t^2}\right)^{-1/2} \exp\left(\frac{\sqrt{c^2t^2 - r^2} - ct}{l}\right) H(ct-r), \quad (46)$$

614 where  $l$  is the scattering mean free path of 5000 m,  $r$  is the distance between  $\mathbf{s}_1$  and  $\mathbf{s}_2$ ,  
 615 and  $H$  is the Heaviside step function. Figure 12 (a) shows the sensitivity kernel at the  
 616 lapse time  $t = 60$  s, which shows two local maxima at the stations. If the damaged area  
 617 is 1 km at the Shinmoe-dake, which is about twice as the crater size, the velocity drop  
 618 within the area is estimated to be about 5%. A trade-off exists between  $\delta c$  and the dam-  
 619 aged area.

620 We considered three possible origins of the localized seismic velocity changes: (i)  
 621 stress sensitivity of the edifice in a linear elastic regime, (ii) density perturbation due to  
 622 the magma intrusion, and (iii) damage accumulation near the crater. We already showed  
 623 that the stress sensitivity in this region is small, though past studies (e.g., Sens-Schönfelder  
 624 et al., 2014) have shown that stress changes due to the increased pressure of the magma  
 625 reservoir could cause the observable seismic velocity change. Moreover, no other infla-  
 626 tion/deflation sources were observed before the 2011 Shinmoe-dake eruption. Next, we  
 627 considered density perturbation, as in the case of the precipitation effect. Kozono et al.  
 628 (2013) estimated the erupted volume based on geodetic and satellite observations. The  
 629 total extruded volume of dense rock equivalence was estimated to about  $3 \times 10^7$  m<sup>3</sup>, and  
 630 the density was 2500 kg/m<sup>3</sup>. In order to constrain the upper limit of seismic velocity re-  
 631 duction due the density perturbation, we assumed that the magma was stored at a depth  
 632 shallower than 0.6 km where Rayleigh waves have the greater sensitivity (Figure 5). The  
 633 equation (38) leads to the upper limit of about 0.6% drop in seismic velocity, which is  
 634 significantly smaller than our observations (5%). Therefore we conclude that the observed  
 635 seismic velocity drop with a time scale of about one month near the crater could be caused  
 636 by cumulative damage beyond the linear elastic regime, induced by the pressure exerted  
 637 by the magma reservoir on the edifice (Olivier et al., 2019).

638 The location of the volcanic tremor (TR) source also gives us a clue as to the magma  
 639 or gas movement before the main eruption. Ichihara and Matsumoto (2017) located TR  
 640 sources from seven stations recording continuous volcanic tremor before and during the  
 641 sub-Plinian eruptions using the amplitude distribution. Figure 11(b) shows the source  
 642 depth of TR from January 3rd, 2011, to February 2nd, 2011. Prior to January 2011, the  
 643 TR amplitudes were too small to locate. Before the precursory stage of the eruption, the  
 644 source depths were approximately 2 km. With increased damage, the source depth mi-  
 645 grated upward to around sea level when the precursory stage was initiated. When the  
 646 sub-Plinian eruption started, the decreasing rate of seismic velocity changes became steeper.  
 647 This observation suggests that the magma migration from 2 km to the surface increased  
 648 the damage of the sub-surface material. Figure 12(b) shows the depth section of the source  
 649 locations. They also support the vertical magma migration beneath the summit. The  
 650 sources below 1 km could be biased in the western direction, due to the limited station  
 651 distribution.

652 Ambient noise tomography in this region (Nagaoka, 2020) revealed the magma reser-  
 653 voir imaged as a low S-wave velocity body with a strong radial anisotropy of up to 30%.  
 654 It was located just below the geodetic source, and the horizontal scale was about 15 km  
 655 (Figure 13). Horizontally multilayered sills can explain the strong radial anisotropy with  
 656 and without partial melts. The connection between the sills can enable the horizontal  
 657 magma migration from the magma reservoir to Shinmoe-dake. The geochemical anal-  
 658 ysis (Nakada et al., 2013; Suzuki et al., 2013) showed the basaltic magma was stored at  
 659 the magma reservoir. The viscosity is low enough to develop the sill complex, and the  
 660 mobility is high during the eruption. In January 2011, due to damage, the pressuriza-  
 661 tion of the magma began to decrease the seismic velocity gradually. The pressurization

662 also activated TR activity at depth of 2 km (Figure 13(a)). During this stage, the sili-  
 663 cific magma was mixed with the basaltic magma (Suzuki et al., 2013). Since the viscos-  
 664 ity of the silicic magma is estimated to be high (about  $1.2 \times 10^6$  Pa·s, Suzuki et al., 2013),  
 665 the magma fluid could be isolated.

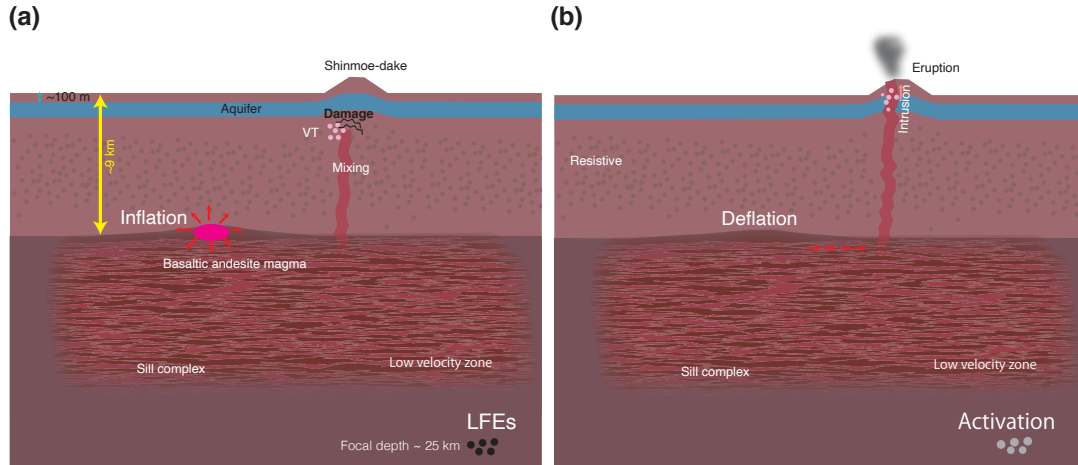


**Figure 13.** Schematic of the 2011 eruption: (a) from one month before until just before the eruption, and (b) during the eruption. LFEs represent low frequency earthquakes (Kurihara et al., 2019), and TR represents volcanic tremor (Ichihara & Matsumoto, 2017).

## 666 8 Conclusions

667 In this study, seismic interferometry was applied to a seismic network around Shinmoe-  
 668 dake to monitor the seismic velocity change for eight years from May 2010 to April 2018.  
 669 We applied the stretching method (Sens-Schönfelder & Wegler, 2006) for a cross-correlation  
 670 function calculated for each pair of stations using continuous ambient noise data. To sep-  
 671 arate the variations of volcanic origin from environmental variations, we developed a new  
 672 technique based on a state-space model: the parameters (e.g., seismic velocity change)  
 673 were estimated by an extended Kalman filter, and the hyper-parameters (the seismic re-  
 674 sponse to the precipitation, the response to the Kumamoto earthquake, and covariances  
 675 of the parameters) were estimated by the Maximum Likelihood Method. The resultant  
 676 seismic velocity changes show clear seasonal variation originating from precipitation as  
 677 well as a drop associated with the 2016 Kumamoto earthquake.

678 After the effects of precipitation and the earthquake were subtracted, most of the  
 679 seismic velocity changes did not show any changes associated with the eruptions. Since  
 680 the strain changes caused by the volumetric change during the 2011 eruption (Nakao et  
 681 al., 2013) were about five microstrains at depths from 0 to 2 km above the source, the  
 682 stress sensitivity of the seismic velocity in a linear elastic regime was significantly smaller  
 683 than other areas (e.g. Takano et al., 2017). The observed lack of sensitivity suggests the  
 684 smaller aspect ratio of crack and less fluid inclusion in the upper crust (Shapiro, 2003),  
 685 which is consistent with the highly resistive body above the volumetric source (Aizawa  
 686 et al., 2014). The P-wave velocity at 3 km is about 5.5 km/s (Tomatsu et al., 2001), and  
 687 the S-wave velocity is about 3.1 km/s (Nagaoka, 2020), indicating small melt fraction  
 688 and crack density.

689 Only one station pair located in the neighborhood of the crater showed a gradual  
 690 decrease in seismic velocity, which preceded the eruption by one month. The maximum  
 691 drop of the seismic velocity was about 0.05% during the 2011 eruption. The sensitivity  
 692 kernel (Pacheco & Snieder, 2005) of this observation suggests that the seismic wave drop  
 693 of about 5% was localized at the crater with a spatial dimension of about one km<sup>2</sup>. In  
 694 this region, P wave travel time tomography revealed a pipe-like structure of high-velocity  
 695 under the summit craters from 1.5 to 0.5 km below sea level (Tomatsu et al., 2001). The  
 696 fluid intrusion started to damage the high-velocity pipe structure one month before the  
 697 eruption. Until January 16th 2011, the source depths of TR were around 2 km (Ichihara  
 698 & Matsumoto, 2017) although the TR amplitudes were too small to locate before Jan-  
 699 uary 2011. With increasing damage, the source depth migrated upward to around sea  
 700 level when the precursory stage started on January 16th. Then, the magma migrated  
 701 from the depth of 2 km to the surface. The magma migrated vertically from the reser-  
 702 voir imaged as a low S-wave velocity body just below the geodetic source.

## 703 Notation

704  $t$ : Days from 1 May 2010 (JST) =  $1, \dots, n$   
 705  $\mathbf{p}$ : A component pair (9 components:  $R - R, R - T, \dots, Z - Z$ ).  
 706  $\tau$ : Lag time of a CCF  
 707  $\phi_t^p(\tau)$ : Observed CCF  
 708  $\mathbf{y}_t^p$ : The data vector consisting of  $\phi_t^p, \tau = (-\tau_e, -\tau_e + 1 \dots - \tau_s, \tau_s \tau_s + 1 \dots \tau_e)$   
 709  $\boldsymbol{\alpha}_t \equiv (\mathbf{A}_t, \gamma_t)^T$ : The state variable  $\boldsymbol{\alpha}_t$  with the amplitude  $A_t$  and stretching factor  $\gamma_t$   
 710  $\mathbf{R}_t \equiv (\mathbf{0}, \mathbf{r}_t)^T$ : Explanatory variables related to precipitation, where  $r_t$  explains the stretch-  
 711 ing factor  
 712  $\mathbf{E}_t \equiv (\mathbf{0}, \mathbf{e}_t)^T$ : Explanatory variables associated with the 2016 Kumamoto earthquake,  
 713 where  $e_t$  explains the stretching factor  
 714  $m^p(\mathbf{A}_t, \gamma_t; \tau)$ : a model of an observed CCF  
 715  $\varphi_{ref}^p(\tau)$ : The reference CCF  
 716  $\mathbf{H}_t \equiv \mathbf{h}_0 \mathbf{I}$ : A prior data covariance matrix, where  $h_0$  is a prior data covariance  
 717  $\mathbf{I}$ : Identity matrix  
 718  $\mathbf{Q}_t$ : A prior model covariance matrix  
 719  $\mathbf{a}_1 \equiv (\mathbf{A}_1, \gamma_1)^T$ : A prior initial value of the state variable  
 720  $\mathbf{P}_1$ : A prior model covariance matrix of the initial value

## 721 Acknowledgments

722 I am grateful to people for maintaining the networks and making the data readily avail-  
 723 able. This work was supported by JSPS KAKENHI Grant Number JP17H02950 and JP17K05625.  
 724 This research made use of ObsPy (Krischer et al., 2015), NumPy (Van Der Walt et al.,  
 725 2011) and SciPy (Virtanen et al., 2019). Figure 1 was prepared with GMT programs (Wessel  
 726 et al., 2013). We thank M. Takeo, Y. Takei and T. Ohminato for the valuable discus-  
 727 sions. We also thank Nori Nakata, Julien Chaput and Rick Aster for their helpful and  
 728 constructive feedback that has improved this manuscript.

## 729 Data and materials availability:

730 We used data from F-net (doi.org/10.17598/nied.0005), Hi-net (doi.org/10  
 731 .17598/nied.0003), V-net (doi.org/10.17598/nied.0006) and K-net (doi.org/10  
 732 .17598/nied.0004), which are managed by the National Research Institute for Earth  
 733 Science and Disaster Prevention (NIED), Japan. In situ precipitation observations were  
 734 obtained from the Automated Meteorological Data Acquisition System (AMeDAS) of  
 735 the Japan Meteorological Agency (JMA) are available at <http://www.data.jma.go.jp/>

736 `obd/stats/etrn/index.php` (in Japanese). F3 solutions of GNSS data are provided by  
 737 Geospatial Information Authority of Japan (<http://www.gsi.go.jp>). Daily CCFs in  
 738 this study are available at zenodo (10.5281/zenodo.2539824). The python code is also  
 739 available at [https://github.com/qnishida/eK1f\\_SI](https://github.com/qnishida/eK1f_SI).

## 740 References

- 741 Aizawa, K., Koyama, T., Hase, H., Uyeshima, M., Kanda, W., Utsugi, M., ...  
 742 Ogawa, Y. (2014). Three-dimensional resistivity structure and magma plumb-  
 743 ing system of the Kirishima Volcanoes as inferred from broadband magnetotel-  
 744 luric data. *Journal of Geophysical Research: Solid Earth*, *119*(1), 198–215. doi:  
 745 10.1002/2013JB010682
- 746 Akaike, H. (1974). A New Look at the Statistical Model Identification. *IEEE*  
 747 *Transactions on Automatic Control*, *19*(6), 716–723. doi: 10.1109/TAC.1974  
 748 .1100705
- 749 Aoki, Y., Segall, P., Kato, T., Cervelli, P., & Shimada, S. (1999). Imaging magma  
 750 transport during the 1997 seismic swarm off the Izu Peninsula, Japan. *Science*,  
 751 *286*(5441), 927–930. doi: 10.1126/science.286.5441.927
- 752 Bensen, G. D., Ritzwoller, M. H., Barmin, M. P., Levshin, A. L., Lin, F., Moschetti,  
 753 M. P., ... Yang, Y. (2007). Processing seismic ambient noise data to obtain re-  
 754 liable broad-band surface wave dispersion measurements. *Geophysical Journal*  
 755 *International*, *169*(3), 1239–1260. doi: 10.1111/j.1365-246X.2007.03374.x
- 756 Brenguier, F., Campillo, M., Hadziioannou, C., Shapiro, N., Nadeau, R. M., &  
 757 Larose, E. (2008). Postseismic relaxation along the san andreas fault at  
 758 parkfield from continuous seismological observations. *Science*, *321*(5895),  
 759 1478–1481.
- 760 Brenguier, F., Campillo, M., Takeda, T., Aoki, Y., Shapiro, N. M., Briand, X.,  
 761 ... Miyake, H. (2014). Mapping pressurized volcanic fluids from in-  
 762 duced crustal seismic velocity drops. *Science*, *345*(6192), 80–82. doi:  
 763 10.1126/science.1254073
- 764 Brenguier, F., Rivet, D., Obermann, A., Nakata, N., Bouoé, P., Lecocq, T., ...  
 765 Shapiro, N. (2016). 4-D noise-based seismology at volcanoes: Ongoing ef-  
 766 forts and perspectives. *Journal of Volcanology and Geothermal Research*, *321*,  
 767 182–195. doi: 10.1016/j.jvolgeores.2016.04.036
- 768 Brenguier, F., Shapiro, N. M., Campillo, M., Ferrazzini, V., Duputel, Z., Coutant,  
 769 O., & Nercessian, A. (2008). Towards forecasting volcanic eruptions using  
 770 seismic noise. *Nature Geoscience*, *1*(2), 126–130. doi: 10.1038/ngeo104
- 771 Budi-Santoso, A., & Lesage, P. (2016). Velocity variations associated with the large  
 772 2010 eruption of Merapi volcano, Java, retrieved from seismic multiplets and  
 773 ambient noise cross-correlation. *Geophysical Journal International*, *206*(1),  
 774 221–240. doi: 10.1093/gji/ggw145
- 775 Colombi, A., Chaput, J., Brenguier, F., Hillers, G., Roux, P., & Campillo, M.  
 776 (2014). On the temporal stability of the coda of ambient noise correla-  
 777 tions. *Comptes Rendus - Geoscience*, *346*(11-12), 307–316. doi: 10.1016/  
 778 j.crte.2014.10.002
- 779 Donaldson, C., Caudron, C., Green, R. G., Thelen, W. A., & White, R. S. (2017).  
 780 Relative seismic velocity variations correlate with deformation at Klauea vol-  
 781 cano. *Science Advances*, *3*(6), e1700219. doi: 10.1126/sciadv.1700219
- 782 Durbin, J., & Koopman, S. J. (2012). *Time Series Analysis by State Space Methods*  
 783 (Second ed.). Oxford University Press. doi: 10.1093/acprof:oso/9780199641178  
 784 .001.0001
- 785 Farr, T. G., Rosen, P. A., Caro, E., Crippen, R., Duren, R., Hensley, S., ... Alsdorf,  
 786 D. (2007). The Shuttle Radar Topography Mission. *Review of Geophysics*,  
 787 *45*(2), RG2004. doi: 10.1029/2005RG000183
- 788 Gassenmeier, M., Sens-Schönfelder, C., Eulenfeld, T., Bartsch, M., Victor, P.,

- 789 Tilmann, F., & Korn, M. (2016). Field observations of seismic velocity  
790 changes caused by shaking-induced damage and healing due to mesoscopic  
791 nonlinearity. *Geophysical Journal International*, *204*(3), 1490–1502. doi:  
792 10.1093/gji/ggv529
- 793 Gomberg, J., & Agnew, D. (1996). The accuracy of seismic estimates of dynamic  
794 strains: An evaluation using strainmeter and seismometer data from Piñon  
795 Flat Observatory, California. *Bulletin of the Seismological Society of America*,  
796 *86*(1 SUPPL. A), 212–220.
- 797 Hendriyana, A., & Tsuji, T. (2019). Migration of Very Long Period Seismicity at  
798 Aso Volcano, Japan, Associated With the 2016 Kumamoto Earthquake. *Geo-  
799 physical Research Letters*, *46*(15), 8763–8771. doi: 10.1029/2019GL082645
- 800 Hillers, G., Ben-Zion, Y., Campillo, M., & Zigone, D. (2015). Seasonal varia-  
801 tions of seismic velocities in the San Jacinto fault area observed with ambient  
802 seismic noise. *Geophysical Journal International*, *202*(2), 920–932. doi:  
803 10.1093/gji/ggv151
- 804 Hillers, G., Husen, S., Obermann, A., Planès, T., Larose, E., & Campillo, M. (2015).  
805 Noise-based monitoring and imaging of aseismic transient deformation induced  
806 by the 2006 Basel reservoir stimulation. *Geophysics*, *80*(4), KS51–KS68. doi:  
807 10.1190/geo2014-0455.1
- 808 Hobiger, M., Wegler, U., Shiomi, K., & Nakahara, H. (2016). Coseismic and post-  
809 seismic velocity changes detected by passive image interferometry: Comparison  
810 of one great and five strong earthquakes in Japan. *Geophysical Journal Inter-  
811 national*, *205*(2), 1053–1073. doi: 10.1093/gji/ggw066
- 812 Ichihara, M., & Matsumoto, S. (2017). Relative Source Locations of Contin-  
813 uous Tremor Before and After the Subplinian Events at Shinmoe-dake,  
814 in 2011. *Geophysical Research Letters*, *44*(21), 10,871–10,877. doi:  
815 10.1002/2017GL075293
- 816 Kagiya, T., Utada, H., Uyeshima, M., Masutani, F., Kanda, W., Tanaka, Y., ...  
817 Mishina, M. (1996). Resistivity Structure of the Central and the Southeastern  
818 Part of Kirishima Volcanoes. *Bulltin of the volcanological society of Japan*,  
819 *41*(5), 215–225. doi: 10.18940/kazan.41.5.215
- 820 Kaneshima, S., Kawakatsu, H., Matsubayashi, H., Sudo, Y., Tsutsui, T., Ohminato,  
821 T., ... Iidaka, T. (1996). Mechanism of Phreatic Eruptions at Aso Volcano  
822 Inferred from Near-Field Broadband Seismic Observations. *Science*, *273*(5275),  
823 643–645. doi: 10.1126/science.273.5275.643
- 824 Kato, A., Nakamura, K., & Hiyama, Y. (2016). The 2016 Kumamoto earthquake  
825 sequence. *Proceedings of the Japan Academy Series B: Physical and Biological  
826 Sciences*, *92*(8), 358–371. doi: 10.2183/pjab.92.359
- 827 Kim, D., & Lekic, V. (2019). Groundwater Variations From Autocorrelation and  
828 Receiver Functions. *Geophysical Research Letters*, *722*–729. doi: 10.1029/  
829 2019GL084719
- 830 Kozono, T., Ueda, H., Ozawa, T., Koyaguchi, T., Fujita, E., Tomiya, A., & Suzuki,  
831 Y. J. (2013). Magma discharge variations during the 2011 eruptions of  
832 Shinmoe-dake volcano, Japan, revealed by geodetic and satellite observations.  
833 *Bull. Volcanol.*, *75*(3), 1–13. doi: 10.1007/s00445-013-0695-4
- 834 Krischer, L., Megies, T., Barsch, R., Beyreuther, M., Lecocq, T., Caudron, C., &  
835 Wassermann, J. (2015). ObsPy: A bridge for seismology into the scien-  
836 tific Python ecosystem. *Computational Science and Discovery*, *8*(1). doi:  
837 10.1088/1749-4699/8/1/014003
- 838 Kurihara, R., Obara, K., Takeo, A., & Tanaka, Y. (2019). Deep Low-Frequency  
839 Earthquakes Associated With the Eruptions of Shinmoe-dake in KirishimaVol-  
840 canoes. *Journal of Geophysical Research: Solid Earth*, 2019JB018032. doi:  
841 10.1029/2019JB018032
- 842 Lecocq, T., Longuevergne, L., Pedersen, H. A., Brenguier, F., & Stammer, K.  
843 (2017). Monitoring ground water storage at mesoscale using seismic noise:

- 844 30 years of continuous observation and thermo-elastic and hydrological model-  
845 ing. *Sci. Rep.*, 7(1), 1–16. doi: 10.1038/s41598-017-14468-9
- 846 Machacca, R., Lesage, P., Larose, E., Lacroix, P., & Anccasi, R. (2019). De-  
847 tection of pre-eruptive seismic velocity variations at an andesitic volcano  
848 using ambient noise correlation on 3-component stations: Ubinas vol-  
849 cano, Peru, 2014. *Journal of Volcanology and Geothermal Research*. doi:  
850 10.1016/j.jvolgeores.2019.05.014
- 851 Maeda, T., Obara, K., Furumura, T., & Saito, T. (2011). Interference of long-period  
852 seismic wavefield observed by dense hi-net array in japan. *Journal of Geophysi-  
853 cal Research*, 116.
- 854 Malinverno, A., & Briggs, V. A. (2004). Expanded uncertainty quantification in  
855 inverse problems: Hierarchical Bayes and empirical Bayes. *Geophysics*, 69(4),  
856 1005–1016. doi: 10.1190/1.1778243
- 857 Miyazawa, M. (2011). Propagation of an earthquake triggering front from the 2011  
858 Tohoku-Oki earthquake. *Geophysical Research Letters*, 38(23), n/a–n/a. doi:  
859 10.1029/2011GL049795
- 860 Nagaoka, Y. (2020). *Study on seismic velocity structure beneath active volcanoes by  
861 seismic interferometry* (PhD). The university of Tokyo.
- 862 Nagaoka, Y., Nishida, K., Aoki, Y., & Takeo, M. (2010). Temporal change of phase  
863 velocity beneath Mt. Asama, Japan, inferred from coda wave interferometry.  
864 *Geophysical Research Letters*, 37(22), 1–5. doi: 10.1029/2010GL045289
- 865 Nakada, S., Nagai, M., Kaneko, T., Suzuki, Y., & Maeno, F. (2013). The outline  
866 of the 2011 eruption at Shinmoe-dake (Kirishima), Japan. *Earth, Planets and  
867 Space*, 65(6), 475–488. doi: 10.5047/eps.2013.03.016
- 868 Nakamichi, H., Yamanaka, Y., Terakawa, T., Horikawa, S., Okuda, T., & Ya-  
869 mazaki, F. (2013). Continuous long-term array analysis of seismic records  
870 observed during the 2011 Shinmoedake eruption activity of Kirishima vol-  
871 cano, southwest Japan. *Earth, Planets and Space*, 65(6), 551–562. doi:  
872 10.5047/eps.2013.03.002
- 873 Nakao, S., Morita, Y., Yakiwara, H., Oikawa, J., Ueda, H., Takahashi, H., ... Iguchi,  
874 M. (2013). Volume change of the magma reservoir relating to the 2011  
875 Kirishima Shinmoe-dake eruption—Charging, discharging and recharging  
876 process inferred from GPS measurements. *Earth, Planets and Space*, 65(6),  
877 505–515. doi: 10.5047/eps.2013.05.017
- 878 Nimiya, H., Ikeda, T., & Tsuji, T. (2017). Spatial and temporal seismic velocity  
879 changes on Kyushu Island during the 2016 Kumamoto earthquake. *Science Ad-  
880 vances*, 3(11), e1700813. doi: 10.1126/sciadv.1700813
- 881 Nishida, K., Kawakatsu, H., & Obara, K. (2008). Three-dimensional crustal S wave  
882 velocity structure in Japan using microseismic data recorded by Hi-net tilt-  
883 meters. *Journal of Geophysical Research: Solid Earth*, 113(B10), B10302. doi:  
884 10.1029/2007JB005395
- 885 Niu, F., Silver, P. G., Daley, T. M., Cheng, X., & Majer, E. L. (2008). Preseismic  
886 velocity changes observed from active source monitoring at the parkfield safod  
887 drill site. *Nature*, 454(7201), 204.
- 888 Obermann, A., & Hillers, G. (2019). Chapter Two - Seismic time-lapse interferom-  
889 etry across scales. In C. Schmelzbach (Ed.), *Advances in seismology* (Vol. 60,  
890 pp. 65–143). Elsevier. doi: 10.1016/bs.agph.2019.06.001
- 891 Obermann, A., Planes, T., Larose, E., Sens-Schonfelder, C., & Campillo, M. (2013).  
892 Depth sensitivity of seismic coda waves to velocity perturbations in an elastic  
893 heterogeneous medium. *Geophysical Journal International*, 194(1), 372–382.  
894 doi: 10.1093/gji/ggt043
- 895 Ogiso, M., Yomogida, K., & Katsumata, K. (2005). Recursive travel-time inver-  
896 sion: A tool for real-time seismic tomography. *Earth, Planets Sp.*, 57(6), 477–  
897 489. doi: 10.1186/BF03352582
- 898 Okada, Y. (1992). Internal deformation due to shear and tensile faults in a half-

- 899 space. *Bulletin - Seismological Society of America*, *82*(2), 1018–1040.
- 900 Olivier, G., Brenguier, F., Carey, R., Okubo, P., & Donaldson, C. (2019). Decrease  
901 in Seismic Velocity Observed Prior to the 2018 Eruption of Kilauea Volcano  
902 With Ambient Seismic Noise Interferometry. *Geophysical Research Letters*,  
903 *46*(7), 3734–3744. doi: 10.1029/2018GL081609
- 904 Pacheco, C., & Snieder, R. (2005). Time-lapse travel time change of multiply  
905 scattered acoustic waves. *The Journal of the Acoustical Society of America*,  
906 *118*(3), 1300–1310. doi: 10.1121/1.2000827
- 907 Poupinet, G., Ellsworth, W., & Frechet, J. (1984). Monitoring velocity variations  
908 in the crust using earthquake doublets: An application to the calaveras fault,  
909 california. *Journal of Geophysical Research: Solid Earth*, *89*(B7), 5719–5731.
- 910 Rivet, D., Brenguier, F., & Cappa, F. (2015). Improved detection of preruptive  
911 seismic velocity drops at the Piton de La Fournaise volcano. *Geophysical Re-*  
912 *search Letters*, 1–8. doi: 10.1002/2015GL064835.Received
- 913 Rivet, D., Campillo, M., Shapiro, N. M., Cruz-Atienza, V., Radiguet, M., Cotte, N.,  
914 & Kostoglodov, V. (2011). Seismic evidence of nonlinear crustal deformation  
915 during a large slow slip event in Mexico. *Geophysical Research Letters*, *38*(8),  
916 3–7. doi: 10.1029/2011GL047151
- 917 Sandanbata, O., Obara, K., Maeda, T., Takagi, R., & Satake, K. (2015). Sudden  
918 changes in the amplitude-frequency distribution of long-period tremors at Aso  
919 volcano, southwest Japan. *Geophysical Research Letters*, *42*(23), 10256–10262.  
920 doi: 10.1002/2015GL066443
- 921 Segall, P., & Matthews, M. (1997). Time dependent inversion of geodetic data.  
922 *Journal of Geophysical Research: Solid Earth*, *102*(B10), 22391–22409. doi: 10  
923 .1029/97JB01795
- 924 Sens-Schönfelder, C., & Eulenfeld, T. (2019). Probing the in situ Elastic Nonlin-  
925 earity of Rocks with Earth Tides and Seismic Noise. *Phys. Rev. Lett.*, *122*(13),  
926 138501. doi: 10.1103/PhysRevLett.122.138501
- 927 Sens-Schönfelder, C., Pomponi, E., & Peltier, A. (2014). Dynamics of Piton de  
928 la Fournaise volcano observed by passive image interferometry with multiple  
929 references. *Journal of Volcanology and Geothermal Research*, *276*, 32–45. doi:  
930 10.1016/j.jvolgeores.2014.02.012
- 931 Sens-Schönfelder, C., & Wegler, U. (2006). Passive image interferometry and sea-  
932 sonal variations of seismic velocities at Merapi Volcano, Indonesia. *Geophysical*  
933 *Research Letters*, *33*(21), 1–5. doi: 10.1029/2006GL027797
- 934 Shapiro, S. A. (2003). Elastic piezosensitivity of porous and fractured rocks. *Geo-*  
935 *physics*, *68*(2), 482–486. doi: 10.1190/1.1567215
- 936 Snieder, R., Sens-Schönfelder, C., & Wu, R. (2017). The time dependence of rock  
937 healing as a universal relaxation process, a tutorial. *Geophysical Journal Inter-*  
938 *national*, *208*(1), 1–9. doi: 10.1093/gji/ggw377
- 939 Suzuki, Y., Yasuda, A., Hokanishi, N., Kaneko, T., Nakada, S., & Fujii, T. (2013).  
940 Syneruptive deep magma transfer and shallow magma remobilization during  
941 the 2011 eruption of Shinmoe-dake, Japan-Constraints from melt inclusions  
942 and phase equilibria experiments. *Journal of Volcanology and Geothermal*  
943 *Research*, *257*, 184–204. doi: 10.1016/j.jvolgeores.2013.03.017
- 944 Takano, T., Nishimura, T., & Nakahara, H. (2017). Seismic velocity changes concen-  
945 trated at the shallow structure as inferred from correlation analyses of ambient  
946 noise during volcano deformation at Izu-Oshima, Japan. *Journal of Geophys-*  
947 *ical Research: Solid Earth*, *122*(8), 6721–6736. doi: 10.1002/2017JB014340
- 948 Takano, T., Nishimura, T., Nakahara, H., Ohta, Y., & Tanaka, S. (2014). Seismic  
949 velocity changes caused by the Earth tide: Ambient noise correlation analyses  
950 of small-array data. *Geophysical Research Letters*, *41*(17), 6131–6136. doi:  
951 10.1002/2014GL060690
- 952 Takano, T., Nishimura, T., Nakahara, H., Ueda, H., & Fujita, E. (2019). Sen-  
953 sitivity of Seismic Velocity Changes to the Tidal Strain at Different Lapse

- 954 Times: Data Analyses of a Small Seismic Array at Izu-Oshima Volcano.  
 955 *Journal of Geophysical Research: Solid Earth*, *124*(3), 3011–3023. doi:  
 956 10.1029/2018JB016235
- 957 Takeo, M., Maehara, Y., Ichihara, M., Ohminato, T., Kamata, R., & Oikawa, J.  
 958 (2013). Ground deformation cycles in a magma-effusive stage, and sub-Plinian  
 959 and Vulcanian eruptions at Kirishima volcanoes, Japan. *Journal of Geophysical*  
 960 *Research: Solid Earth*, *118*(9), 4758–4773. doi: 10.1002/jgrb.50278
- 961 Takeuchi, H., & Saito, M. (1972). Seismology: Surface Waves and Free Oscilla-  
 962 tions. In B. A. Bolt (Ed.), *Methods in computational physics* (Vol. 11, pp. 217–  
 963 295). Academic Press, New York.
- 964 Talwani, P., Chen, L., & Gahalaut, K. (2007). Seismogenic permeability, ks. *Journal*  
 965 *of Geophysical Research: Solid Earth*, *112*(B7).
- 966 Tarantola, A., & Valette, B. (1982). Generalized nonlinear inverse problems solved  
 967 using the least squares criterion. *Reviews of Geophysics*, *20*(2), 219. doi: 10  
 968 .1029/RG020i002p00219
- 969 Tomatsu, T., Kumagai, H., & Dawson, P. B. (2001). Tomographic inversion  
 970 of P-wave velocity and Q structures beneath the Kirishima volcanic com-  
 971 plex, Southern Japan, based on finite difference calculations of complex  
 972 traveltimes. *Geophysical Journal International*, *146*(3), 781–794. doi:  
 973 10.1046/j.1365-246X.2001.00491.x
- 974 Tsukamoto, K., Aizawa, K., Chiba, K., Kanda, W., Uyeshima, M., Koyama, T., ...  
 975 Kishita, T. (2018). Three-Dimensional Resistivity Structure of Iwo-Yama Vol-  
 976 cano, Kirishima Volcanic Complex, Japan: Relationship to Shallow Seismicity,  
 977 Surface Uplift, and a Small Phreatic Eruption. *Geophysical Research Letters*,  
 978 *45*(23), 12,821–12,828. doi: 10.1029/2018GL080202
- 979 Ueda, H., Kozono, T., Fujita, E., Kohno, Y., Nagai, M., Miyagi, Y., & Tanada, T.  
 980 (2013). Crustal deformation associated with the 2011 Shinmoe-dake eruption  
 981 as observed by tiltmeters and GPS. *Earth, Planets and Space*, *65*(6), 517–525.  
 982 doi: 10.5047/eps.2013.03.001
- 983 Van Der Walt, S., Colbert, S. C., & Varoquaux, G. (2011). The numpy array: a  
 984 structure for efficient numerical computation. *Computing in Science & Engi-  
 985 neering*, *13*(2), 22–30.
- 986 Virtanen, P., Gommers, R., Oliphant, T. E., Haberland, M., Reddy, T., Courn-  
 987 peau, D., ... Contributors, S. . . (2019). SciPy 1.0–Fundamental Algorithms  
 988 for Scientific Computing in Python. *arXiv e-prints*, arXiv:1907.10121.
- 989 Wang, Q.-Y., Brenguier, F., Campillo, M., Lecointre, A., Takeda, T., & Aoki,  
 990 Y. (2017). Seasonal crustal seismic velocity changes throughout Japan.  
 991 *Journal of Geophysical Research: Solid Earth*, *122*(10), 7987–8002. doi:  
 992 10.1002/2017JB014307
- 993 Wang, Q. Y., Campillo, M., Brenguier, F., Lecointre, A., Takeda, T., & Hashima, A.  
 994 (2019). Evidence of Changes of Seismic Properties in the Entire Crust Beneath  
 995 Japan After the Mw 9.0, 2011 Tohoku-oki Earthquake. *Journal of Geophysical*  
 996 *Research: Solid Earth*, *124*(8), 8924–8941. doi: 10.1029/2019JB017803
- 997 Weaver, R., Froment, B., & Campillo, M. (2009). On the correlation of non-  
 998 isotropically distributed ballistic scalar diffuse waves. *The Journal of the*  
 999 *Acoustical Society of America*, *126*(4), 1817–26. doi: 10.1121/1.3203359
- 1000 Weaver, R., Hadziioannou, C., Larose, E., & Campillo, M. (2011). On the precision  
 1001 of noise correlation interferometry. *Geophysical Journal International*, *185*(3),  
 1002 1384–1392. doi: 10.1111/j.1365-246X.2011.05015.x
- 1003 Weaver, R., & Lobkis, O. (2000). Temperature dependence of diffuse field phase. *Ul-  
 1004 trasonics*, *38*(1), 491–494. doi: 10.1016/S0041-624X(99)00047-5
- 1005 Wegler, U., Nakahara, H., Sens-Schönfelder, C., Korn, M., & Shiomi, K. (2009).  
 1006 Sudden drop of seismic velocity after the 2004 Mw 6.6 mid-Niigata earthquake,  
 1007 Japan, observed with Passive Image Interferometry B06305. *Journal of Geo-  
 1008 physical Research: Solid Earth*, *114*(6), 1–11. doi: 10.1029/2008JB005869

- 1009 Wegler, U., & Sens-Schönfelder, C. (2007). Fault zone monitoring with passive image  
 1010 interferometry. *Geophysical Journal International*, *168*(3), 1029–1033.
- 1011 Wessel, P., Smith, W. H. F., Scharroo, R., Luis, J., & Wobbe, F. (2013). Generic  
 1012 mapping tools: Improved version released. *Eos, Transactions American Geo-*  
 1013 *physical Union*, *94*(45), 409-410. doi: 10.1002/2013EO450001
- 1014 Yamada, T., Ueda, H., Mori, T., & Tanada, T. (2019). Tracing Volcanic Activ-  
 1015 ity Chronology from a Multiparameter Dataset at Shinmoedake Volcano  
 1016 (Kirishima), Japan. *Journal of Disaster Research*, *14*(5), 687–700. doi:  
 1017 10.20965/jdr.2019.p0687
- 1018 Yamamura, K., Sano, O., Utada, H., Takei, Y., Nakao, S., & Fukao, Y. (2003).  
 1019 Long-term observation of in situ seismic velocity and attenuation. *Jour-*  
 1020 *nal of Geophysical Research: Solid Earth*, *108*(B6), 1–15. doi: 10.1029/  
 1021 2002JB002005
- 1022 Zhu, C., Byrd, R. H., Lu, P., & Nocedal, J. (1994). Fortran subroutines for large-  
 1023 scale bound constrained optimization. *ACM Trans Math Softw*, *23*(4), 550–  
 1024 60.

## 1025 Appendix A Calculation of the likelihood

1026 For an efficient evaluation of the likelihood defined by equation (32), calculation  
 1027 of the determinant of a large matrix  $\mathbf{F}_t$  ( $N \times N$  matrix) becomes the bottleneck. To re-  
 1028 duce the calculations, we rewrote the definition of the likelihood as follows. Since  $\mathbf{Z}_t \hat{\mathbf{P}}_{t|t-1} \mathbf{Z}_t^T$   
 1029 is the symmetric matrix, it can be diagonalized by the unitary matrix  $\mathbf{U}$  as

$$1030 \mathbf{U}^t \mathbf{F}_t \mathbf{U} = \mathbf{\Lambda}, \quad (\text{A1})$$

1031 where the eigen matrix  $\mathbf{\Lambda}$  can be written

$$1032 \mathbf{\Lambda} \equiv \begin{pmatrix} \lambda_1 & 0 & 0 & \cdots & 0 \\ 0 & \lambda_2 & 0 & \cdots & 0 \\ 0 & 0 & 0 & \cdots & 0 \\ \vdots & \vdots & \vdots & \ddots & \vdots \\ 0 & 0 & 0 & \cdots & 0 \end{pmatrix}, \quad (\text{A2})$$

1033 Since the rank of  $\mathbf{Z}_t \hat{\mathbf{P}}_{t|t-1} \mathbf{Z}_t^T$  is 2, the other  $N - 2$  eigen values are zeros.

1034 Then the determinant can be written by

$$1035 \det(\mathbf{F}_t) = \det(\mathbf{U}^T \mathbf{F}_t \mathbf{U}) = \det(\mathbf{\Lambda} + h_0 \mathbf{I}) = (\lambda_1 + h_0)(\lambda_2 + h_0)h_0^{N-2}. \quad (\text{A3})$$

1036 Here we consider the eigen values of  $\mathbf{Z}_t \hat{\mathbf{P}}_{t|t-1} \mathbf{Z}_t^T$ . For a given eigen vector  $\mathbf{x}_i$  for eigen  
 1037 value  $\lambda_i$ ,

$$1038 \mathbf{Z}_t \hat{\mathbf{P}}_{t|t-1} \mathbf{Z}_t^T \mathbf{x} = \lambda_i \mathbf{x}_i. \quad (\text{A4})$$

1039 Multiply both sides of each equation by  $\mathbf{Z}_t$

$$1040 \mathbf{Z}_t^T \mathbf{Z}_t \hat{\mathbf{P}}_{t|t-1} \mathbf{Z}_t^T \mathbf{x} = \lambda_i \mathbf{Z}_t^T \mathbf{x}_i. \quad (\text{A5})$$

1041 Since this equation can be interpreted as an eigen value problem for the smaller matrix  
 1042  $\mathbf{Z}_t^T \mathbf{Z}_t \hat{\mathbf{P}}_{t|t-1}$  ( $2 \times 2$  matrix), we can obtain these efficiently.